

# Structures and pH-sensing mechanism of the proton-activated chloride channel

<https://doi.org/10.1038/s41586-020-2875-7>

Zheng Ruan<sup>1,4</sup>, James Osei-Owusu<sup>2,4</sup>, Juan Du<sup>1</sup>, Zhaozhu Qiu<sup>2,3</sup>✉ & Wei Lü<sup>1</sup>✉

Received: 4 April 2020

Accepted: 14 August 2020

Published online: 4 November 2020

 Check for updates

The proton-activated chloride channel (PAC) is active across a wide range of mammalian cells and is involved in acid-induced cell death and tissue injury<sup>1–3</sup>. PAC has recently been shown to represent a novel and evolutionarily conserved protein family<sup>4,5</sup>. Here we present two cryo-electron microscopy structures of human PAC in a high-pH resting closed state and a low-pH proton-bound non-conducting state. PAC is a trimer in which each subunit consists of a transmembrane domain (TMD), which is formed of two helices (TM1 and TM2), and an extracellular domain (ECD). Upon a decrease of pH from 8 to 4, we observed marked conformational changes in the ECD–TMD interface and the TMD. The rearrangement of the ECD–TMD interface is characterized by the movement of the histidine 98 residue, which is, after acidification, decoupled from the resting position and inserted into an acidic pocket that is about 5 Å away. Within the TMD, TM1 undergoes a rotational movement, switching its interaction partner from its cognate TM2 to the adjacent TM2. The anion selectivity of PAC is determined by the positively charged lysine 319 residue on TM2, and replacing lysine 319 with a glutamate residue converts PAC to a cation-selective channel. Our data provide a glimpse of the molecular assembly of PAC, and a basis for understanding the mechanism of proton-dependent activation.

Acidic pH is crucial for the function of intracellular organelles in the secretory and endocytic pathways. It is also one of the pathological hallmarks of many diseases, including cerebral and cardiac ischaemia, cancer, infection and inflammation. The activity of PAC is stimulated by the lowering of extracellular pH and has been recorded in a wide range of mammalian cells<sup>1</sup>. By mediating the influx of Cl<sup>–</sup> and subsequent cell swelling, PAC is implicated in acid-induced cell death<sup>2,3</sup>. We and others recently used unbiased RNA interference screens<sup>4,5</sup> to identify a novel gene, *PAC1* (also known as *TMEM206*), that encodes the PAC channel. Our functional studies revealed that PAC has a key role in acid-induced neuronal cell death in vitro and in ischaemic brain injury in mice<sup>4,6</sup>.

With no obvious sequence homology to other membrane proteins, PAC represents a completely new family of ion channels<sup>4,5</sup>. PAC is highly conserved across vertebrates and is predicted to have two transmembrane helices<sup>4,5</sup>, similar to the acid-sensing ion channel (ASIC) and the epithelial sodium channel (ENaC)<sup>7,8</sup>. Although the structure and function of ASIC have been extensively studied<sup>7,9–12</sup>, the architecture of PAC and the mechanisms that underlie its pH sensing and anion selectivity are unknown. To address these questions, we determined structures of human PAC using single-particle cryo-electron microscopy (cryo-EM) combined with patch-clamp electrophysiological studies.

## Structural determination

PAC is activated at a pH below 5.5 at room temperature, and is maximally stimulated by protons at around pH 4.6–4<sup>1</sup>. We determined

cryo-EM structures of PAC reconstituted in lipid nanodiscs at pH 8 (pH8-PAC) and pH 4 (pH4-PAC) with estimated resolutions of 3.60 and 3.73 Å, respectively (Extended Data Figs. 1a–c, 2, 3, Extended Data Table 1). The maps were of sufficient quality to carry out de novo model building of the protein (Fig. 1, Extended Data Fig. 4a–d, Extended Data Table 1). The cytoplasmic N and C termini (residues 1–60 and 339–350 in pH8-PAC and 1–52 and 340–350 in pH4-PAC) are disordered in our cryo-EM maps.

## Overall architecture

PAC is a trimer. It has a small, ball-shaped ECD sitting on top of a slim and elongated TMD that contains two transmembrane helices (TM1 and TM2) in each subunit (Fig. 1a, b, e, f). This trimeric two-transmembrane-helix architecture is reminiscent of ASIC (Extended Data Fig. 5a–e) and ENaC<sup>7,8</sup>. The ECD of PAC is heavily glycosylated, with four N-glycosylation sites in each subunit (Fig. 1c, g)—consistent with a previous report<sup>5</sup> and a deglycosylation assay (Extended Data Fig. 1d).

Alkaline and acidic pH yielded two PAC structures with distinct shapes—pH4-PAC is shorter and bulkier than pH8-PAC, and they differ mainly at the TMD and the ECD–TMD interface. At pH 8, the TM1 helix runs nearly parallel to and forms interactions only with its cognate TM2 (Fig. 1b, d). When the pH drops to 4, TM1 switches its interaction from its cognate TM2 to the adjacent TM2 (Fig. 1f, h). This domain-swapped movement of TM1 has not, to our knowledge, been observed in any

<sup>1</sup>Department of Structural Biology, Van Andel Institute, Grand Rapids, MI, USA. <sup>2</sup>Department of Physiology, Johns Hopkins University School of Medicine, Baltimore, MD, USA.

<sup>3</sup>Solomon H. Snyder Department of Neuroscience, Johns Hopkins University School of Medicine, Baltimore, MD, USA. <sup>4</sup>These authors contributed equally: Zheng Ruan, James Osei-Owusu.

✉e-mail: zhaozhu@jhmi.edu; wei.lu@vai.org

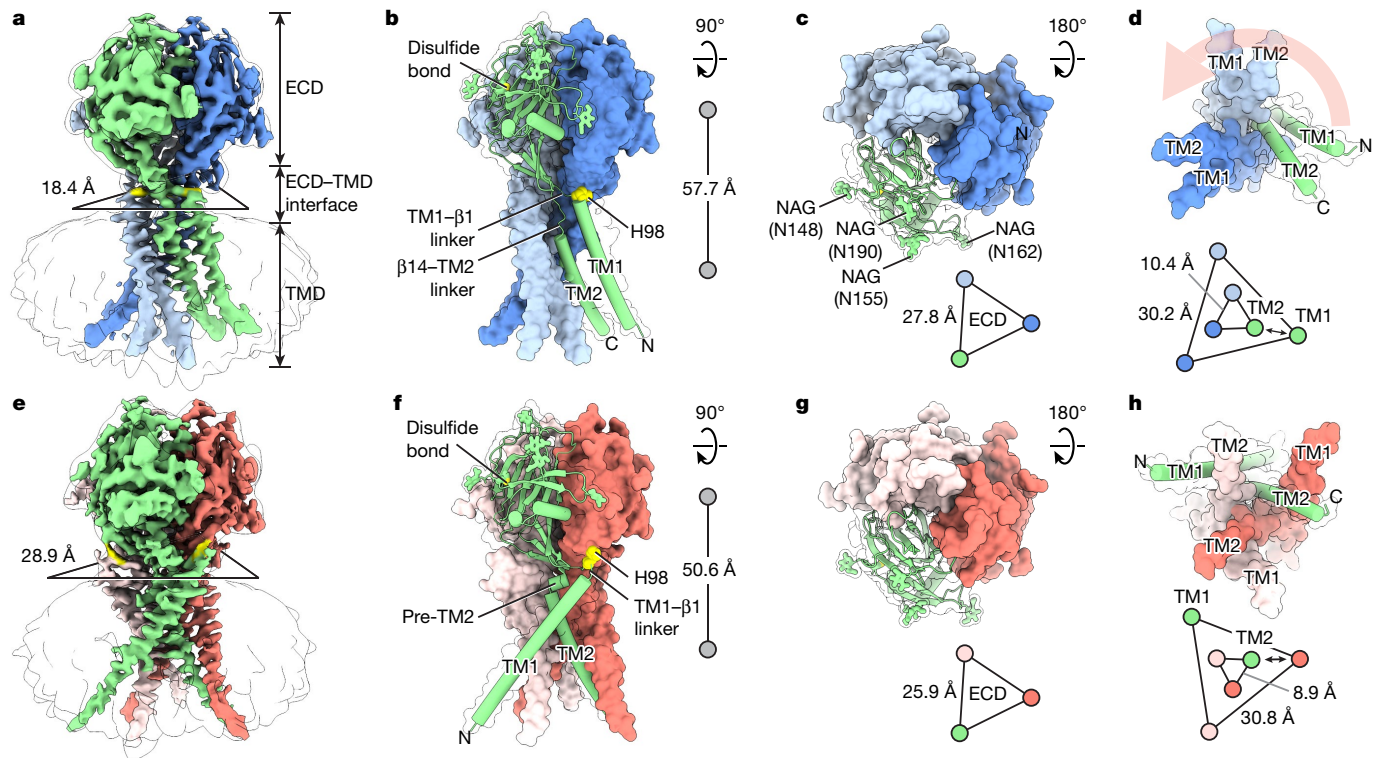


**Fig. 1 | Overall architecture of PAC. a, e,** Cryo-EM maps of pH8-PAC and pH4-PAC viewed parallel to the membrane. The map refined without using a mask is shown as a transparent envelope. The horizontal dimension of the ECD–TMD interface is represented by the distance between the C $\alpha$  atoms of adjacent His98 residues. The density for His98 is coloured in yellow in the pH8-PAC (a) and pH4-PAC (e) maps. **b, f,** Atomic models of pH8-PAC and pH4-PAC. The green subunit is shown as a cartoon and the other two subunits are shown in surface representation. The distances between the centre of mass of the ECD and of the TMD in pH8-PAC (b) and pH4-PAC (f) are shown on the right. **c, g,** The ECDs of pH8-PAC and pH4-PAC viewed from the extracellular side. Four putative

glycosylation sites (Asn148, Asn155, Asn162 and Asn190) are labelled in c. The distances between the centre of mass of the ECDs of each subunit in pH8-PAC (c) and pH4-PAC (g) are shown by the triangles. **d, h,** The TMDs of pH8-PAC and pH4-PAC viewed from the intracellular side. A light salmon arrow in d indicates the rotation of TM1 of PAC after acidification to pH 4. The relative position and distance of TM1 and TM2 in pH8-PAC (d) and pH4-PAC (h), which are represented by the C $\alpha$  atoms of Iso73 and Lys319, respectively, are shown at the bottom. The double-headed arrow indicates the interaction between TM1 and TM2.

other two-transmembrane-helix channels,<sup>12,13</sup> implying a novel gating mechanism.

The ECD–TMD interface consists of part of the TM1 helix on the extracellular side and two linkers that connect the TMD and the ECD—the TM1– $\beta$ 1 linker and the  $\beta$ 14–TM2 linker. This interface differs substantially between the two PAC structures (Fig. 1b, f). At pH 8, TM1 and the short TM1– $\beta$ 1 linker hold the adjacent ECD through an ‘anchor’ residue, His98, while the  $\beta$ 14–TM2 linker is extended as a loop close to the pore axis (Fig. 1b). At pH 4, the  $\beta$ 14–TM2 linker is remodelled into a short pre-TM2 helix, and the TM1– $\beta$ 1 linker moves outward, causing a vertical compression and an expansion of the ECD–TMD interface (Fig. 1a, b, e, f, Supplementary Video 1). In tandem with the rearrangement of the ECD–TMD interface, the ECD at pH 4 shows a vertical movement towards the TMD and a contraction towards the pore axis, resulting in a shorter overall structure and a more compact ECD in comparison to that at pH 8 (Fig. 1b, c, f, g).

### Structure of single subunits

At pH 8, each PAC protomer adopts an arm-like structure, with the ECD as the hand, the ECD–TMD interface as the wrist and the TMD as the forearm (Extended Data Fig. 4e). The hand-like ECD is composed of a palm, a finger, a thumb and a  $\beta$ -ball domain, all of which consist of  $\beta$ -strands except for the thumb domain, which contains two short  $\alpha$ -helices (Extended Data Fig. 4e–g). The finger and the  $\beta$ -ball domains are connected by a disulfide bond (Cys128–Cys149), forming a rigid

structure that occupies the peripheral region of the ECD. The connection between the ECD and the TMD is achieved by the TM1– $\beta$ 1 and  $\beta$ 14–TM2 linkers, which together form the wrist domain.

The TMD consists of two transmembrane helices, TM1 and TM2, at the N terminus and C terminus of the protein, respectively. TM1 contains mostly hydrophobic residues and makes direct contacts with the lipid bilayer. TM2 contains both hydrophilic and hydrophobic residues and lines the ion-conducting pore. Although the ECD mostly maintains its conformation in both pH states, the ECD–TMD interface and TMD differ substantially at pH 4 and pH 8, characterized by the distinct conformations of His98 and TM1 (Extended Data Fig. 4e, f). At pH 8, TM1 is approximately parallel to TM2, whereas at pH 4, the two transmembrane helices form an angle of 64°.

The TM2 helix of PAC is a continuous  $\alpha$ -helix and differs from the ASIC TM2, which has a characteristic two-segment structure and a Gly-Ala-Ser belt<sup>10</sup> (Extended Data Fig. 5b, e). The ECD of PAC shows strong similarities to the  $\beta$ -sheet core of the ECD in ASIC, despite sharing limited protein-sequence identity (Extended Data Figs. 5e, 6). Notably, the PAC ECD lacks the large exterior helical structures of the ASIC ECD, which are involved in pH sensing<sup>14</sup> (Extended Data Figs. 5a–d, 6), so PAC must have a different pH-sensing mechanism.

### Channel assembly

The major interactions between PAC subunits occur at the ECD, the ECD–TMD interface and in the upper part of the TMD. The lower part

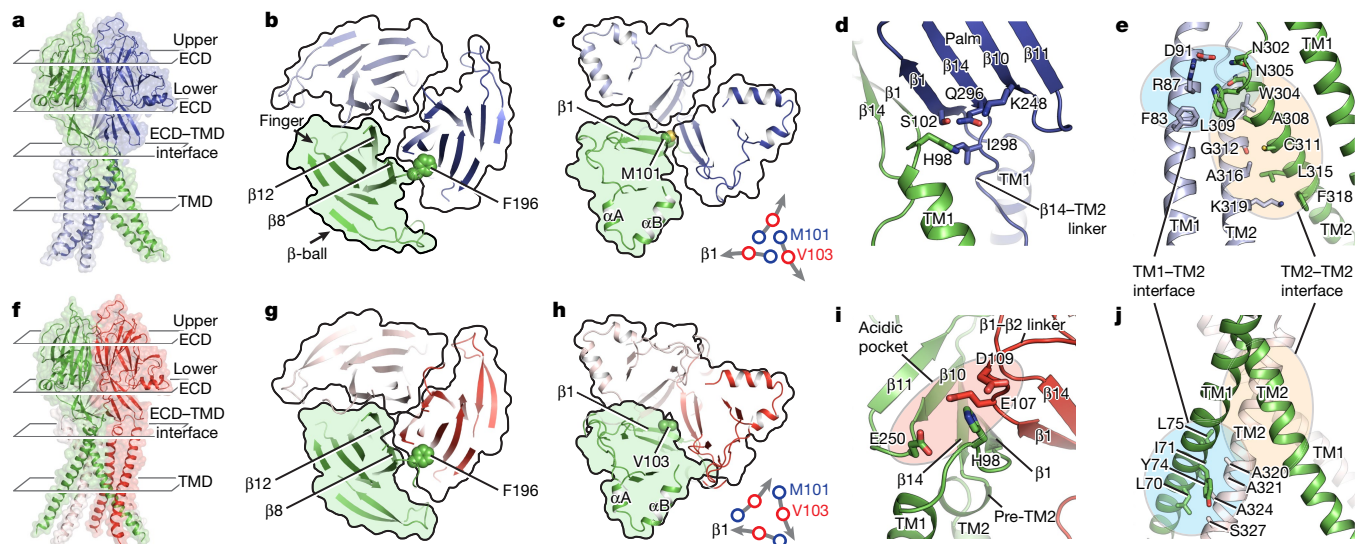


**Fig. 2 | Intersubunit interfaces.** Each row represents the same view of pH8-PAC (top row; **a–e**) and pH4-PAC (bottom row; **f–j**). **a, f**, The overall structure of PAC shown in cartoon and surface representation. The ECD is divided into the upper ECD and lower ECD for discussion. **b, g**, The upper ECD viewed from the extracellular side. Phe196, which mediates the intersubunit interaction in the upper ECD, is shown as spheres. **c, h**, The lower ECD viewed

from the extracellular side. At pH 8, Met101 at the beginning of the  $\beta$ 1 strand is in the centre of the lower ECD (**c**, bottom right). At pH 4, the lower ECD undergoes a clockwise inward rotation so that Val103 in the middle of the  $\beta$ 1 strand moves to the centre of the lower ECD (**h**, bottom right). **d, i**, The ECD-TMD interface viewed parallel to the membrane. **e, j**, The interaction interfaces at the TMD.

of the TMD lacks extensive interactions and is thus flexible. Analysis of the conformational changes at the ECD revealed a rigid-body contraction of the entire ECD and an iris-like rotation of the lower ECD (Supplementary Video 1). We thus looked at both the upper ECD (finger and  $\beta$ -ball domains) and the lower ECD (palm and thumb domains) to study their intersubunit interfaces (Fig. 2a, f).

At pH 8, both the upper and the lower ECD have loose intersubunit interfaces with an obvious gap between subunits (Fig. 2b, c). The upper ECD has two major intersubunit interactions. The first is formed between the adjacent  $\beta$ 8 and  $\beta$ 12 strands that run approximately parallel to each other. The second is formed between the  $\beta$ 6– $\beta$ 7 linker and the adjacent finger domain, where the Phe196 residue on the  $\beta$ 6– $\beta$ 7 linker is inserted into the finger domain, forming both hydrophobic and cation– $\pi$  interactions (Fig. 2b, g, Extended Data Fig. 1e). Substitution of Phe196 with an alanine residue (F196A) yielded a misassembled mutant protein that exhibited a markedly decreased channel activity compared to the wild type (Extended Data Fig. 1f, g). This suggests that the upper ECD has an important role in channel assembly. The lower ECD has a single major interface at the centre, where the three Met101 residues on the N terminus of the  $\beta$ 1 strand tightly interact with each other. This interface disconnects the central pore from the ECD to the TMD (Fig. 2c). At pH 4, the gaps in both the upper and the lower ECDs are mostly filled, creating extensive interactions between subunits (Fig. 2g, h). Moreover, in the centre of the lower ECD, owing to the iris-like rotation of the ECD from pH 8 to pH 4, the Val103 residue in the middle of the  $\beta$ 1 strand now mediates the contact (Fig. 2h).

The intersubunit contact at the ECD-TMD interface is mediated through His98 at the TM1– $\beta$ 1 linker. At pH 8, His98 is surrounded by hydrophilic and hydrophobic residues of the  $\beta$ 1 and  $\beta$ 14 strands of the adjacent ECD, constituting a resting ECD-TMD interface (Fig. 2d). At pH 4, this interface is remodelled; His98 interacts with a pocket formed by residues in the  $\beta$ 10– $\beta$ 11 linker of its cognate ECD and in the  $\beta$ 1– $\beta$ 2 linker of the adjacent ECD (Fig. 2i). Because this pocket is constructed solely of negatively charged residues, we call it an ‘acidic pocket’.

At the TMD, PAC has two major intersubunit interfaces (Fig. 2e, j): the TM1–TM2 interface and the TM2–TM2 interface. At pH 8, both interfaces are near the extracellular part of the TMD. At pH 4, the TM2–TM2

interface remains mostly unchanged, but the TM1–TM2 interface slips towards the intracellular side as a result of the domain-swapped movement of TM1.

### Ion-conducting pathway and selectivity

The PAC channel has a central pore along the symmetry axis with wide openings at the extracellular and intracellular ends in both pH states (Fig. 3a–d). Within the TMD, the ion-conducting pore is lined by TM2 and the  $\beta$ 14–TM2 linker (Fig. 3b, d). At pH 8, the ion-conducting pore is occluded at several positions (Fig. 3e, g), thus representing a high-pH resting closed state. At pH 4 (Fig. 3f, g), the intracellular part of the pore has an enlarged radius of 0.82 Å, but is still not wide enough to allow the permeation of  $\text{Cl}^-$  ions, thus representing a low-pH protonated non-conducting state. We found that PAC exhibits a strong outward rectification such that either the open probability or the single-channel conductance is low at 0 mV, the voltage at which the cryo-EM structures were determined (Fig. 3h). Moreover, PAC showed a marked desensitization after prolonged treatment with a pH 4 solution (Extended Data Fig. 7a–f). Therefore, we suggest that a closed pore in the pH4-PAC structure represents either a pre-open state or a desensitized state.

To reveal the molecular determinants that are responsible for the anion selectivity of PAC, we examined the positively charged residues within the ion-conducting pore, all of which are located in the intracellular half of the TM2 helix. The Lys319 residue appears to be an ideal candidate, because it is immediately below the intracellular restriction site (Leu315) and forms a positively charged ‘triad’ around the intracellular entry point (Fig. 3e, f). In line with this hypothesis, we found that a charge-reversing mutation (K319E) converted PAC from an anion-selective to a cation-selective channel with a pronounced inwardly rectifying current (Fig. 3h–j, Extended Data Fig. 8a, b). By contrast, mutation of two other lysine residues, K325E and K329E, resulted in mutant proteins that behaved similarly to wild-type PAC (Extended Data Fig. 8a–e). The crucial role of Lys319 is further supported by its conservation across species (Extended Data Fig. 6), and by the fact that PAC(K319C) is not functional<sup>5</sup>. Together, our data provide evidence that Lys319 is the determinant of anion selectivity for PAC.

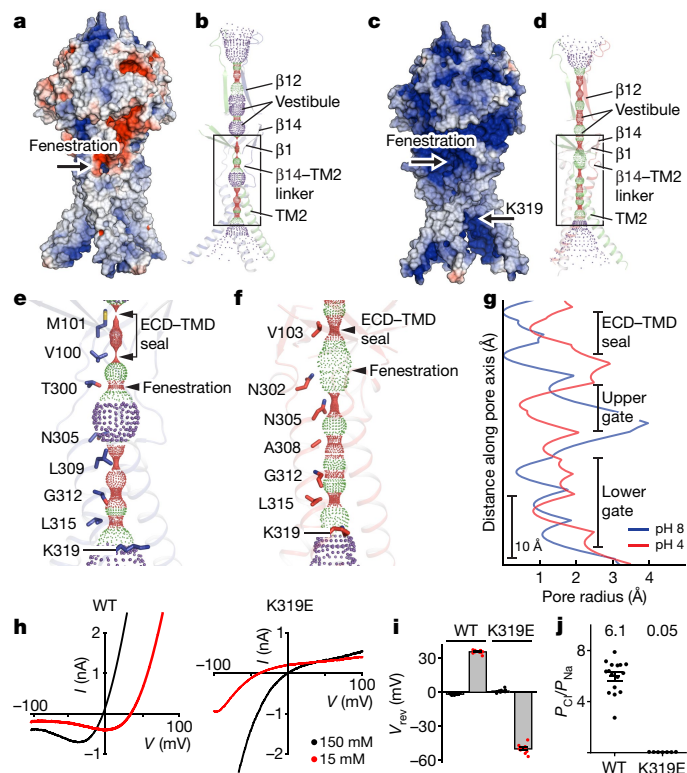


**Fig. 3 | Ion-conducting pathways and anion selectivity.** **a, c,** pH8-PAC (**a**) and pH4-PAC (**c**) in surface representation, coloured according to the electrostatic surface potential from  $-3$  to  $3$  kT/e (red to blue). Titratable residues are assigned to their predominant protonation state at pH 8 (**a**) or pH 4 (**c**) based on PROPKA. **b, d,** The pore profiles of pH8-PAC (**b**) and pH4-PAC (**d**) models along the symmetry axis. Pore-lining residues are shown. **e, f,** Enlargements of the boxed areas in **b** (**e**) and **d** (**f**), respectively. The positions of the ECD–TMD seal and fenestration site are labelled. **g,** Pore radius plots of the profiles in **e, f**. **h,** The representative current ( $I$ )–voltage ( $V$ ) relationship for wild-type (WT) PAC and PAC(K319E). The pipette solution contains 150 mM NaCl; the bath solution contains 150 mM (black) or 15 mM (red) NaCl. **i,** The reversal potential ( $V_{rev}$ ) of wild-type PAC and PAC(K319E) from recordings in **h** ( $n = 16$  (wild type) and  $n = 7$  (K319E)). Data are mean  $\pm$  s.e.m. Individual data points are shown as dots. **j,** The relative  $Cl^-/Na^+$  permeability ( $P_{Cl^-}/P_{Na^+}$ ) for wild-type PAC ( $n = 15$ ) and PAC(K319E) ( $n = 11$ ) calculated from current induced at pH 5 and 100 mV. Data are mean  $\pm$  s.e.m. of the permeability ratio. Individual data points are shown as solid dots. The average  $P_{Cl^-}/P_{Na^+}$  permeability values are indicated at the top for each construct.

In the ECD, the pore along the symmetry axis has a large vestibule in the middle (Fig. 3b, d). This vestibule is constricted at the ECD–TMD interface by an ECD–TMD seal in both the pH8-PAC and the pH4-PAC structures (Fig. 3e–g, Extended Data Fig. 8f, i). This leads to the question of how ions might enter the ion-conducting pore from the extracellular side. Just below the seal, we observed three lateral fenestrations that connect to the central pore. Fenestrations at similar locations have been defined as an ion-entry point in both the ASIC and P2X channels<sup>9,13,15</sup>. At pH 8, the fenestration in PAC is formed by the extracellular portion of the TM1 helix and the  $\beta$ 14–TM2 linker of the adjacent subunit (Extended Data Fig. 8f). The entrance is surrounded by several negatively charged residues, making it unfavourable for conducting anions (Extended Data Fig. 8g). At pH 4, a different fenestration is established by the  $\beta$ 1 strand and the pre-TM2 helix in the adjacent subunit (Extended Data Fig. 8i). The fenestration at pH 4 is wider than that at pH 8, and has several positively charged residues lining the entry point, rendering it favourable for anions (Extended Data Fig. 8i, j). To provide evidence that these fenestrations could be extracellular ion-entry points in PAC, we performed molecular dynamics simulations and found that the fenestrations in

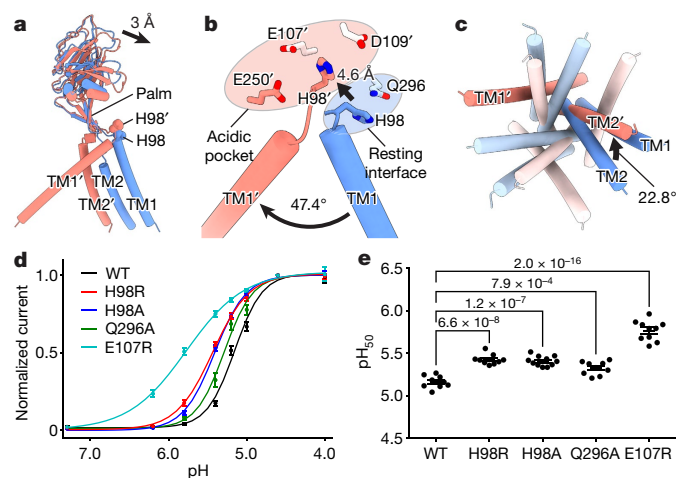


**Fig. 4 | Mechanisms of pH sensing and channel activation.** **a,** Superposition of a single subunit of pH8-PAC (blue) and pH4-PAC (red) aligned using the ECD palm domain. The 3 Å centre-of-mass distance indicates the rigid-body movement of the ECD. **b,** Close-up view of the conformational change in the ECD–TMD interface in **a**. Structural elements and residues in the pH4-PAC structure are labelled with a prime symbol. Residues from adjacent subunits are coloured in bright and light colours, respectively. At pH 8, His98 interacts with Gln296. At pH 4, the side chain of His98 interacts with an acidic pocket. **c,** Comparison of the TMD viewed from the intracellular side. The structures of pH8-PAC (blue) and pH4-PAC (red) are aligned using the ECD. **d,** pH dose-response curve of wild-type PAC and various PAC mutants. Data are mean  $\pm$  s.e.m. of the current at 100 mV, normalized to pH 4.6-induced current ( $n = 10$  (wild type), H98R, E107R),  $n = 9$  (H98A) and  $n = 11$  (Q296A)). The Hill coefficients for wild-type PAC and PAC(E107R) are  $2.44 \pm 0.18$  and  $1.18 \pm 0.19$  (mean  $\pm$  s.e.m.), respectively. **e,** pH<sub>50</sub> value estimated from the pH dose-response curve. The centre and error bar represent the estimated pH<sub>50</sub> value and s.e.m. from the nonlinear fitting in **d**. A one-way analysis of variance (ANOVA) with Bonferroni post-hoc test was used to determine the significance ( $P$  values are indicated).

the pH4-PAC structure are hydrated, whereas those in the pH8-PAC structure are less accessible to solvent (Extended Data Fig. 8h, k). Our data suggest that the lateral fenestrations could be an extracellular ion-entry point that is common to two-transmembrane-helix channels<sup>9,13,15</sup>. This agrees with a previous report in which treatment with a thiol-reactive reagent, MTSES, partially inhibited the ion-channel activity of PAC when Thr306—which is part of the fenestration—was replaced by a cysteine residue<sup>5</sup>.

## Mechanisms of pH sensing and channel activation

To elucidate the pH-sensing mechanism of PAC, we compared the structures of pH8-PAC and pH4-PAC. We focused on the ECD and the ECD–TMD interface, because PAC is activated by extracellular acid. Superimposing a single subunit revealed that, upon protonation, the major motion of the extracellular region occurred at the ECD–TMD interface, whereas the ECD showed minor rigid-body movement (Fig. 4a). This suggests that the ECD–TMD interface probably participates in pH sensing. We hypothesized that the His98 residue in the TM1– $\beta$ 1 linker is one of the key pH sensors, because it showed a large movement from the high-pH resting state to the low-pH proton-bound state and because its side-chain  $pK_a$  value is close to the pH<sub>50</sub> (pH of half-maximal activation) value of PAC<sup>16</sup> (Extended Data Fig. 9a).

At pH 8, His98 is in close contact with the Gln296, Iso298 and Ser102 residues of the adjacent ECD. We speculated that the side chain of His98 forms a hydrogen bond with the side-chain amine group of Gln296, which locks the TM1 helix in a conformation parallel to its cognate TM2 helix (Fig. 4a, b). To investigate whether the interaction between

His98 and Gln296 is critical for stabilizing the channel in a resting closed state, we engineered a disulfide bond connecting these two residues. Indeed, double mutation of both His98 and Gln296 to cysteine (H98C/Q296C) fixed His98 in the resting position and thus rendered PAC insensitive to pH, whereas the control serine double mutant (H98S/Q296S) showed increased pH sensitivity (Extended Data Fig. 9b–f). At pH 4, the protonated His98 is decoupled from Gln296 and flipped into the acidic pocket, which is 4.6 Å away (Fig. 4b). The acidic pocket is formed by Glu107, Asp109 and Glu250, and interacts favourably with the protonated His98 residue because Asp109 is predicted to remain unprotonated at pH 4 (Extended Data Fig. 9a). The flipping of His98 pulls TM1 away from its cognate TM2 and creates a new interface with the TM2 of the adjacent subunit (Fig. 4b). Concurrent with a 47.4° swing of TM1, the pore-lining TM2 undergoes a counterclockwise rotation of 22.8° when viewed from the intracellular side (Fig. 4b, c).

We hypothesized that the flipping of His98 from the resting position to the acidic pocket is a critical element for the proton-induced activation of the PAC channel. To test this hypothesis, we first generated mutants of His98 and its interacting partner in the pH8-PAC structure (Gln296) and examined their pH sensitivity (Fig. 4d, e). H98R, H98A and Q296A mutants all resulted in an increased pH sensitivity by disengaging the hydrogen bond between His98 and Gln296, which supports the idea that the decoupling of protonated His98 from the resting interface has a role in channel activation. However, the H98A and H98R mutants showed a similar  $\text{pH}_{50}$  value, which is unexpected because an alanine residue would be less attracted by the acidic pocket than an arginine residue. This might be because an arginine residue at position 98 caused additional conformational changes rather than a simple side-chain substitution. Next we studied Glu107, which is close to His98 in the pH4-PAC structure. Mutation of Glu107 to arginine (E107R) not only markedly increased the pH sensitivity but also decreased the Hill coefficient of the pH dose–response curve (Fig. 4d, e). As Glu107 has a predicted  $\text{p}K_a$  value of around 6 in the pH4-PAC structure (Extended Data Fig. 9a), it probably also participates in PAC pH sensing. The E107R mutation might cause a rearrangement of the acidic pocket, which could lead to an altered interaction with His98. Consequently, the activation of the channel might require fewer protons, resulting in an increased pH sensitivity.

## Discussion

Our work on PAC provides a glimpse of the molecular structures and pH-sensing mechanism of a proton-activated chloride channel (Extended Data Fig. 9g). Similarly to ASIC<sup>12,14,17–19</sup>, the pH-sensing mechanism of PAC is almost certainly determined by multiple residues, because several tested mutations altered the pH sensitivity but none of them abolished it, and because titratable residues are distributed throughout the ECD (Extended Data Fig. 9a). Our structural and functional data suggest that the pH4-PAC structure represents a proton-bound pre-open state or a proton-bound desensitized state. We acknowledge the limits of using a proton-bound non-conducting conformation to discuss the activation mechanism, because the TMD may

differ from that in an open state. Indeed, cysteine mutants of multiple pore-lining residues in TM2 (for example, Ala316, Leu315, Gly312) can still be accessed by the thiol-reactive reagent MTSES from the extracellular side<sup>5</sup>, indicating that the ion-conducting pore and lateral fenestrations in an open state are probably substantially larger than in either of the present structures. Further studies are required to develop a thorough understanding of this family of proton-sensitive ion channels.

## Online content

Any methods, additional references, Nature Research reporting summaries, source data, extended data, supplementary information, acknowledgements, peer review information; details of author contributions and competing interests; and statements of data and code availability are available at <https://doi.org/10.1038/s41586-020-2875-7>.

1. Capurro, V. et al. Functional analysis of acid-activated  $\text{Cl}^-$  channels: properties and mechanisms of regulation. *Biochim. Biophys. Acta* **1848**, 105–114 (2015).
2. Wang, H. Y., Shimizu, T., Numata, T. & Okada, Y. Role of acid-sensitive outwardly rectifying anion channels in acidosis-induced cell death in human epithelial cells. *Pflügers Arch.* **454**, 223–233 (2007).
3. Sato-Numata, K., Numata, T. & Okada, Y. Temperature sensitivity of acid-sensitive outwardly rectifying (ASOR) anion channels in cortical neurons is involved in hypothermic neuroprotection against acidotoxic necrosis. *Channels* **8**, 278–283 (2014).
4. Yang, J. et al. PAC, an evolutionarily conserved membrane protein, is a proton-activated chloride channel. *Science* **364**, 395–399 (2019).
5. Ullrich, F. et al. Identification of TMEM206 proteins as pore of PAORAC/ASOR acid-sensitive chloride channels. *eLife* **8**, e49187 (2019).
6. Osei-Owusu, J., Yang, J., Del Carmen Vitery, M., Tian, M. & Qiu, Z. PAC proton-activated chloride channel contributes to acid-induced cell death in primary rat cortical neurons. *Channels* **14**, 53–58 (2020).
7. Jasti, J., Furukawa, H., Gonzales, E. B. & Gouaux, E. Structure of acid-sensing ion channel 1 at 1.9 Å resolution and low pH. *Nature* **449**, 316–323 (2007).
8. Noreng, S., Bharadwaj, A., Posert, R., Yoshioka, C. & Bacongus, I. Structure of the human epithelial sodium channel by cryo-electron microscopy. *eLife* **7**, e39340 (2018).
9. Gonzales, E. B., Kawate, T. & Gouaux, E. Pore architecture and ion sites in acid-sensing ion channels and P2X<sub>2</sub> receptors. *Nature* **460**, 599–604 (2009).
10. Bacongus, I., Bohlen, C. J., Goehring, A., Julius, D. & Gouaux, E. X-ray structure of acid-sensing ion channel 1-snake toxin complex reveals open state of a  $\text{Na}^+$ -selective channel. *Cell* **156**, 717–729 (2014).
11. Yoder, N. & Gouaux, E. Divalent cation and chloride ion sites of chicken acid sensing ion channel 1a elucidated by X-ray crystallography. *PLoS ONE* **13**, e0202134 (2018).
12. Yoder, N., Yoshioka, C. & Gouaux, E. Gating mechanisms of acid-sensing ion channels. *Nature* **555**, 397–401 (2018).
13. Mansoor, S. E. et al. X-ray structures define human P2X<sub>3</sub> receptor gating cycle and antagonist action. *Nature* **538**, 66–71 (2016).
14. Vullo, S. et al. Conformational dynamics and role of the acidic pocket in ASIC pH-dependent gating. *Proc. Natl Acad. Sci. USA* **114**, 3768–3773 (2017).
15. Gao, C. et al. Roles of the lateral fenestration residues of the P2X<sub>2</sub> receptor that contribute to the channel function and the deactivation effect of ivermectin. *Purinergic Signal.* **11**, 229–238 (2015).
16. Lambert, S. & Oberwinkler, J. Characterization of a proton-activated, outwardly rectifying anion channel. *J. Physiol.* **567**, 191–213 (2005).
17. Liechti, L. A. et al. A combined computational and functional approach identifies new residues involved in pH-dependent gating of ASIC1a. *J. Biol. Chem.* **285**, 16315–16329 (2010).
18. Smith, E. S. J., Zhang, X., Cadiou, H. & McNaughton, P. A. Proton binding sites involved in the activation of acid-sensing ion channel ASIC2a. *Neurosci. Lett.* **426**, 12–17 (2007).
19. Paukert, M., Chen, X., Pollehn, G., Schindelin, H. & Gründer, S. Candidate amino acids involved in H<sup>+</sup> gating of acid-sensing ion channel 1a. *J. Biol. Chem.* **283**, 572–581 (2008).

**Publisher's note** Springer Nature remains neutral with regard to jurisdictional claims in published maps and institutional affiliations.

© The Author(s), under exclusive licence to Springer Nature Limited 2020

## Methods

### Data reporting

No statistical methods were used to predetermine sample size. The experiments were not randomized and the investigators were not blinded to allocation during experiments and outcome assessment.

### Constructs and mutagenesis

For protein expression and purification, the human PAC gene (*PACCI*; Uniprot ID Q9H813) from our previous study<sup>4</sup> was subcloned into a pEG BacMam vector<sup>20</sup> with a thrombin cutting site, enhanced green fluorescent protein (eGFP) and 8×His tag in the C terminus. The pIRES2-eGFP vector containing *PACCI* was used for whole-cell patch-clamp recordings<sup>4</sup>. Site-directed mutagenesis was performed using the QuikChange site-directed mutagenesis protocol (Agilent) and confirmed by Sanger sequencing.

### Mammalian cell culture, protein expression, purification and nanodisc reconstitution

For small-scale protein expression, adherent tsA201 cells were maintained in Dulbecco's modified Eagle medium (DMEM) supplemented with 10% fetal bovine serum (FBS) at 37 °C. When the cell density reached approximately 80% confluence, transient transfection was performed by incubating the plasmid DNA and Lipofectamine-2000 reagent (Thermo Fisher Scientific) in Opti-MEM medium (Thermo Fisher Scientific) using manufacturer-provided protocols. Sodium butyrate (10 mM) was added to the adherent cells 24 h after transfection. The cells were then maintained at 30 °C to boost protein expression. The next day, the adherent cells were washed with 20 mM Tris, 150 mM NaCl, pH 8.0 (TBS) buffer, collected and stored at -80 °C.

For large-scale protein expression, we used the Bac-to-Bac baculovirus expression system<sup>21</sup>. Specifically, plasmid expressing wild-type PAC was transfected into DH10 $\alpha$  cells to produce the bacmid. Purified bacmid was transfected into adherent Sf9 cells using Cellfectin II reagent (Thermo Fisher Scientific) to produce P1 virus. P2 virus was then generated by infecting suspension Sf9 cells with the P1 virus at a 1:5,000 (v/v) ratio. The expression of PAC protein was induced by infecting tsA201 suspension cells in FreeStyle 293 medium (Gibco) with 7.5% P2 virus. After 8–12 h, sodium butyrate (5 mM) was added to the infected suspension cells and the temperature was adjusted to 30 °C. Suspension tsA201 cells were collected 70 h after infection and stored at -80 °C.

Mammalian cells infected with PAC were suspended in TBS buffer (150 mM NaCl, 20 mM Tris HCl, pH 8.0) supplemented with a protease inhibitor cocktail (1 mM phenylmethylsulfonyl fluoride, 2 mM pepstatin, 0.8  $\mu$ M aprotinin and 2  $\mu$ g ml<sup>-1</sup> leupeptin) and lysed by sonication. Cell debris was removed by centrifugation at 3,000g for 10 min. The membrane fraction was pooled by ultracentrifugation of the supernatant for 1 h at 186,000g. The membrane was then Dounce-homogenized and solubilized in TBS buffer with 1% glyco-diosgenin (GDN) and the protease inhibitor cocktail. After 1 h, the sample was ultracentrifuged for 1 h at 186,000g. The supernatant was applied to 2 ml talon resin preequilibrated with TBS buffer with 0.02% GDN. The resin was washed with 20 ml TBS buffer with 0.02% GDN and 20 mM imidazole. The protein was eluted with 8 ml TBS buffer with 0.02% GDN and 250 mM imidazole. The eluent was concentrated to 500  $\mu$ l using a 100-kDa concentrator (MilliporeSigma). MSP3D1 protein and soybean lipid (SBL) extract were mixed with the PAC protein sample using a molar ratio of 3:400:1 (MSP3D1:SBL:PAC). Three rounds of biobead incubation were carried out to facilitate nanodisc reconstitution. The volume of the mixture was then expanded to 12.5 ml so that the imidazole concentration was 10 mM. Empty nanodiscs were removed by passing the mixture through talon resin a few times. MSP3D1-PAC was eluted using TBS buffer containing 250 mM imidazole and concentrated to 500  $\mu$ l. Thrombin (0.01 mg ml<sup>-1</sup>) was then added to the eluent to cleave eGFP at 4 °C overnight. The mixture was further purified by size-exclusion chromatography

(SEC) using TBS as the running buffer. Peak fractions were combined and concentrated to 4 mg ml<sup>-1</sup> before grid freezing.

### Cryo-grid preparation

The purified PAC nanodisc protein is in TBS buffer at pH 8. The pH 4 condition was made by adding 1 M acetic acid (pH 3.5) buffer to the purified PAC nanodisc sample at a 1:20 v/v ratio. Fluorinated octyl maltoside (0.5 mM) was added to the sample to help reduce protein unfolding in the air–water interface. Quantifoil grids (Au 1.2/1.3 or Au 2/1, 300 mesh) were glow-discharged for 30 s. A cryo-grid was made using the VitroBotMark III kept at 18 °C and 100% humidity. A volume of 2.5  $\mu$ l of the PAC nanodisc protein sample was loaded to the grid, blotted for 1.5 s, plunge-frozen into liquid ethane and transferred into liquid nitrogen for storage.

### Cryo-EM data collection

Cryo-EM data were collected using a FEI Titan Krios transmission electron microscope equipped with a Gatan K2 Summit direct electron detector. Automated data acquisition was facilitated by SerialEM software in super-resolution counting mode<sup>22</sup>. Each raw movie stack consists of 40 frames with a total dose of 49.6 e<sup>-</sup>/Å<sup>2</sup> for 8 s. Nominal defocus values were set to range from -1.2 to -1.9  $\mu$ m.

### Single-particle data analysis

For both the pH8-PAC and the pH4-PAC dataset, raw movies were first motion-corrected using MotionCorr v.1.2.1 (ref. <sup>23</sup>). The contrast transfer function (CTF) of each micrograph was estimated using Gctf v.1.06 (ref. <sup>24</sup>) or CTFIND<sup>25</sup>. Template-based particle picking was conducted using Gautomatch v.0.53 (<https://www2.mrc-lmb.cam.ac.uk/download/gautomatch-053/>). Junk particles were sorted by two rounds of two-dimensional (2D) classification in RELION v.3.0 (ref. <sup>26</sup>).

For the pH8-PAC dataset, particles belonging to the 2D class averages with features were selected for ab initio three-dimensional (3D) reconstruction in cryoSPARC v.0.6.5 (ref. <sup>27</sup>). The resulting map was then used as the template for 3D classification using RELION v.3.0 with C<sub>1</sub> symmetry. Class averages with high-resolution features were combined and refined by imposing C<sub>3</sub> symmetry. A solvent mask was generated and was used for all subsequent refinement steps. Bayesian polishing was conducted to refine the beam-induced motion of the particle set, resulting in a map at 4.0-Å resolution<sup>28</sup>.

We noticed that the size of the nanodiscs was not homogeneous, which could lead to inaccuracy of particle alignment. In addition, the cytosolic side of the TMD is flexible, which could also influence particle alignment. To address these potential problems, we subtracted the nanodisc signal and further classified the particles without image alignment. A subsequent 3D refinement allowed us to obtain a map at 3.60 Å for PAC. Likewise, we also attempted to only include signals from the ECD and part of the TMD close to the ECD. This strategy allowed us to obtain a reconstruction at 3.36 Å. The pH 8 data-processing workflow is summarized in Extended Data Fig. 2a.

For the pH4-PAC dataset, the initial 3D classification was performed using the pH8-PAC map (low-pass-filtered to 50 Å) as the reference without imposing symmetry. Particles belonging to 3D classes with high-resolution features were pooled and refined using C<sub>3</sub> symmetry. This yielded a reconstruction at 5.8 Å. We then reclassified the particles using this map (low-pass-filtered to 50 Å) and imposed C<sub>3</sub> symmetry. Subsequent refinement on reasonable 3D classes allowed us to obtain a reconstruction at 4.6-Å resolution. Finally, a third 3D classification was initiated by only low-pass-filtering the reference to 7 Å and with C<sub>3</sub> symmetry. This classification helped obtain a homogeneous particle set that gave a reconstruction at 4.2 Å after refinement. We then performed signal subtraction and 3D classification without image alignment by focusing on the ECD and part of the TMD proximal to the ECD. This step allowed us to further push the overall map resolution to 3.73 Å for PAC at pH 4. We also attempted to only refine the ECD and part of the TMD

# Article

for the pH 4 data, which resulted in a map at 3.66-Å resolution. The pH 4 data-processing workflow is summarized in Extended Data Fig. 3a.

## Model building

The pH8-PAC model was built de novo using Coot<sup>29</sup>. Registers were identified by secondary structure prediction from the JPred web server and bulky residues in the density<sup>30</sup>. Both the full map and the ECD-focused map were used during model building. We were able to model residues 61–338 into the map. Extra density observed on Asn148, Asn155, Asn162 and Asn190 in the ECD was modelled as *N*-acetyl-D-glucosamine (NAG) to represent N-linked glycosylation. Real-space refinement was performed in PHENIX to produce the final model<sup>31</sup>.

The pH4-PAC model was first generated by the RosettaEM flexible fitting tools, with the pH8-PAC map as the starting point<sup>32</sup>. The model was then manually adjusted in Coot and subjected to PHENIX real-space refinement<sup>31</sup>. The final model contains residues 53–339 of PAC. Models and maps are visualized using UCSF Chimera, UCSF ChimeraX and PyMOL<sup>33–35</sup>.

## Deglycosylation assay

Adherent tsA201 cells transiently transfected with wild-type PAC-eGFP were solubilized using TBS buffer with 1% GDN for 1 h at 4 °C. The sample was centrifuged at 20,000g for 30 min. Deglycosylation was facilitated by mixing the PNGase F with the supernatant and incubating at room temperature overnight. For the control reaction, the same amount of water was added instead of PNGase F enzyme. The next day, the sample was mixed with 2× SDS sample-loading buffer (Sigma) and resolved by SDS-PAGE electrophoresis. The gel was imaged in the ChemiDoc system by probing the far-red and GFP signal (mUV 680 and 488 nm).

## Molecular dynamics simulations

The structure of PAC in the pH 8 or pH 4 state was used as the starting model. Missing side-chain atoms were fixed using the PDB2PQR utility<sup>36</sup>. Titratable residues were assigned as the predominant protonation state based on the predicted pK<sub>a</sub> value from PROPKA3 at pH 8 or pH 4 (ref. <sup>37</sup>). The membrane orientation of the protein was calculated using the OPM server<sup>38</sup>. Subsequent system preparation was conducted in CHARMM-GUI<sup>39</sup>. POPC lipids were selected to construct the lipid bilayer. The rest of the protein was solvated and neutralized in 150 mM NaCl. The resulting simulation box had dimensions of approximately 87 × 87 × 163 Å.

All-atom molecular dynamics (MD) simulation was carried out using Gromacs v. 2019.2 (ref. <sup>40</sup>). CHARMM36m force field was used to parameterize the MD system<sup>41</sup>. The steepest-descent algorithm was used to minimize the energy of the system so that the  $F_{\max}$  was below 1,000 kJ mol<sup>-1</sup> nm<sup>-1</sup>. The NVT ensemble was then started to keep the temperature of the system at 310 K. Subsequently, the NPT ensemble was enabled by maintaining the system pressure at 1 bar. Protein non-hydrogen atoms and phosphorus groups of POPC were restrained during NVT and NPT equilibration. Production simulation continued from the NPT equilibrated system with the restraints disabled. A Nosé–Hoover thermostat and a Parrinello–Rahman barostat were used to maintain system temperature and pressure, respectively. Hydrogen atoms were constrained using the LINCS algorithms<sup>42</sup>. For efficient GPU acceleration, a Verlet cut-off scheme (12 Å) was enabled to maintain the particle neighbour list. We performed 100-ns simulation for both PAC pH 8 and PAC pH 4 conditions using a time step of 2 fs. Analysis of the MD trajectory was conducted using the utilities inside Gromacs. Specifically, the slice of water molecules in each snapshot was extracted using the gmx select command. The coordinates of oxygen atoms in the water molecules were then projected to the *x/y* plan for visualization.

## pK<sub>a</sub> prediction

We noticed that the pK<sub>a</sub> prediction was very sensitive to the side-chain orientations of the input structure model. To partially account for this

issue, we generated an ensemble of PAC models based on the pH 8 and pH 4 structures using Rosetta. Specifically, the fixed backbone design protocol was used to sample the side-chain rotamers<sup>43</sup>. A total of 1,000 atomic models were built and subjected to pK<sub>a</sub> prediction using PROPKA<sup>37</sup>. The mean and standard deviation of the pK<sub>a</sub> for histidine, glutamate and aspartate residues are provided in Extended Data Fig. 9a.

## Electrophysiology

PAC-knockout HEK293 cells were seeded on coverslips and transfected with wild-type or mutant PAC plasmids using Lipofectamine 2000 (Thermo Fisher Scientific). The cells were recorded around 1 day after transfection. Whole-cell patch-clamp recordings were performed as described previously<sup>4</sup>. The extracellular recording solution contained (in mM): 145 NaCl, 2 KCl, 2 MgCl<sub>2</sub>, 1.5 CaCl<sub>2</sub>, 10 HEPES, 10 glucose (300–310 mOsm/kg; pH 7.3, titrated with NaOH). Acidic extracellular solutions were made of the same ionic composition with 5 mM sodium citrate as the buffer instead of HEPES, and pH was adjusted using citric acid. Solutions were applied locally using a gravity perfusion system with a small tip 100–200 μm away from the recording cell. The intracellular recording solution contained (in mM): 135 CsCl, 1 MgCl<sub>2</sub>, 2 CaCl<sub>2</sub>, 10 HEPES, 5 EGTA, 4 MgATP (280–290 mOsm/kg; pH 7.2, titrated with CsOH). Pipette solution used to observe PAC current at 0 mV contained (in mM): 50 NaCl, 100 sodium gluconate, 10 HEPES (280–290 mOsm/kg; pH 7.2, adjusted with NaOH). Patch pipettes (2–4 MΩ) were pulled with a Model P-1000 multi-step puller (Sutter Instruments).

For selectivity experiments, the extracellular solution used contained (in mM): 15 or 150 NaCl, 10 MES, 10 glucose (osmolality adjusted with mannitol to 300–310 mOsm/kg; pH adjusted with methanesulfonic acid to 5.0). The pipette solution contained (in mM) 150 NaCl, 10 HEPES (280–290 mOsm/kg; pH 7.2, adjusted with NaOH). Voltage ramp pulses were applied every 3 s from –100 to +100 mV at a speed of 1 mV/ms, and a holding potential of 0 mV. The recorded currents were used to generate *I*–*V* curves for reversal potential determination. The permeability ratios were calculated from shifts in the reversal potential using the Goldman–Hodgkin–Katz equation<sup>44</sup>. For the measurement of pH sensitivity, currents were normalized to the maximal current at pH 4.6. The normalized data were then fitted to a pH dose–response curve equation

$$Y = \text{bottom} + \frac{\text{top} - \text{bottom}}{1 + 10^{(X - \text{pH}_{50}) \times \text{HillSlope}}}$$

to estimate the pH<sub>50</sub> and Hill's slope (Hill coefficient). Recordings were done at room temperature with a MultiClamp 700B amplifier and 1550B digitizer (Molecular Devices). Current signals were filtered at 2 kHz and digitized at 10 kHz. Series resistance was compensated for at least 80%. Clampfit v.10.6 and GraphPad Prism v.6 or 7 were used for data analyses.

## Reporting summary

Further information on research design is available in the Nature Research Reporting Summary linked to this paper.

## Data availability

The cryo-EM density maps and coordinates of pH8-PAC and pH4-PAC have been deposited in the Electron Microscopy Data Bank (EMDB) under accession numbers EMD-22403 and EMD-22404 and in the RCSB Protein Data Bank (PDB) under accession codes 7JNA and 7JNC.

20. Goehring, A. et al. Screening and large-scale expression of membrane proteins in mammalian cells for structural studies. *Nat. Protoc.* **9**, 2574–2585 (2014).
21. Haley, E. et al. Expression and purification of the human lipid-sensitive cation channel TRPC3 for structural determination by single-particle cryo-electron microscopy. *J. Vis. Exp.* **143**, e58754 (2019).
22. Mastrorarde, D. N. Automated electron microscope tomography using robust prediction of specimen movements. *J. Struct. Biol.* **152**, 36–51 (2005).

23. Zheng, S. Q. et al. MotionCor2: anisotropic correction of beam-induced motion for improved cryo-electron microscopy. *Nat. Methods* **14**, 331–332 (2017).
24. Zhang, K. Gctf: real-time CTF determination and correction. *J. Struct. Biol.* **193**, 1–12 (2016).
25. Rohou, A. & Grigorieff, N. CTFFIND4: fast and accurate defocus estimation from electron micrographs. *J. Struct. Biol.* **192**, 216–221 (2015).
26. Scheres, S. H. W. RELION: implementation of a Bayesian approach to cryo-EM structure determination. *J. Struct. Biol.* **180**, 519–530 (2012).
27. Punjani, A., Rubinstein, J. L., Fleet, D. J. & Brubaker, M. A. cryoSPARC: algorithms for rapid unsupervised cryo-EM structure determination. *Nat. Methods* **14**, 290–296 (2017).
28. Zivanov, J., Nakane, T. & Scheres, S. H. W. A Bayesian approach to beam-induced motion correction in cryo-EM single-particle analysis. *IUCrJ* **6**, 5–17 (2019).
29. Emsley, P. & Cowtan, K. Coot: model-building tools for molecular graphics. *Acta Crystallogr. D* **60**, 2126–2132 (2004).
30. Drozdetskiy, A., Cole, C., Procter, J. & Barton, G. J. JPred4: a protein secondary structure prediction server. *Nucleic Acids Res.* **43**, W389–W394 (2015).
31. Afonine, P. V. et al. New tools for the analysis and validation of cryo-EM maps and atomic models. *Acta Crystallogr. D* **74**, 814–840 (2018).
32. Wang, R. Y. R. et al. Automated structure refinement of macromolecular assemblies from cryo-EM maps using Rosetta. *eLife* **5**, e17219 (2016).
33. Pettersen, E. F. et al. UCSF Chimera—a visualization system for exploratory research and analysis. *J. Comput. Chem.* **25**, 1605–1612 (2004).
34. Goddard, T. D. et al. UCSF ChimeraX: meeting modern challenges in visualization and analysis. *Protein Sci.* **27**, 14–25 (2018).
35. The PyMOL Molecular Graphics System, v.2.1. (Schrödinger, LLC, 2020).
36. Dolinsky, T. J., Nielsen, J. E., McCammon, J. A. & Baker, N. A. PDB2PQR: an automated pipeline for the setup of Poisson–Boltzmann electrostatics calculations. *Nucleic Acids Res.* **32**, W665–W667 (2004).
37. Olsson, M. H. M., Søndergaard, C. R., Rostkowski, M. & Jensen, J. H. PROPKA3: consistent treatment of internal and surface residues in empirical pK<sub>a</sub> predictions. *J. Chem. Theory Comput.* **7**, 525–537 (2011).
38. Lomize, M. A., Pogozheva, I. D., Joo, H., Mosberg, H. I. & Lomize, A. L. OPM database and PPM web server: resources for positioning of proteins in membranes. *Nucleic Acids Res.* **40**, D370–D376 (2012).
39. Jo, S., Kim, T., Iyer, V. G. & Im, W. CHARMM-GUI: a web-based graphical user interface for CHARMM. *J. Comput. Chem.* **29**, 1859–1865 (2008).
40. Abraham, M. J. et al. Gromacs: high performance molecular simulations through multi-level parallelism from laptops to supercomputers. *SoftwareX* **1–2**, 19–25 (2015).
41. Huang, J. et al. CHARMM36m: an improved force field for folded and intrinsically disordered proteins. *Nat. Methods* **14**, 71–73 (2017).
42. Hess, B. P-LINCS: a parallel linear constraint solver for molecular simulation. *J. Chem. Theory Comput.* **4**, 116–122 (2008).
43. Leaver-Fay, A., Kuhlman, B. & Snoeyink, J. An adaptive dynamic programming algorithm for the side chain placement problem. *Pac. Symp. Biocomput.* **10**, 16–27 (2005).
44. Yang, H. et al. TMEM16F forms a Ca<sup>2+</sup>-activated cation channel required for lipid scrambling in platelets during blood coagulation. *Cell* **151**, 111–122 (2012).
45. Zhang, Y. & Skolnick, J. TM-align: a protein structure alignment algorithm based on the TM-score. *Nucleic Acids Res.* **33**, 2302–2309 (2005).

**Acknowledgements** We thank G. Zhao and X. Meng for support with data collection at the David Van Andel Advanced Cryo-Electron Microscopy Suite; the HPC team of VARI for computational support; and D. Nadziejka for technical editing. W.L. is supported by National Institutes of Health (NIH) grants R56HL144929 and R01NS112363; Z.Q. is supported by a McKnight Scholar Award, a Klingenstein-Simon Scholar Award, a Sloan Research Fellowship in Neuroscience and NIH grants R35GM124824 and R01NS118014; Z.R. is supported by an American Heart Association (AHA) postdoctoral fellowship (grant 20POST35120556); J.O.-O. is supported by an AHA predoctoral fellowship (grant 18PRE34060025); and J.D. is supported by a McKnight Scholar Award, a Klingenstein-Simon Scholar Award, a Sloan Research Fellowship in Neuroscience, a Pew Scholar in the Biomedical Sciences and NIH grant R01NS111031.

**Author contributions** W.L. and Z.Q. supervised the project. Z.R. purified PAC, prepared and screened cryo-EM samples, performed cryo-EM data collection and processing and performed computational simulation. J.O.-O. cloned the PAC constructs and performed electrophysiological studies. Z.R., J.O.-O., J.D., Z.Q. and W.L. contributed to data analysis and manuscript preparation.

**Competing interests** The authors declare no competing interests.

#### Additional information

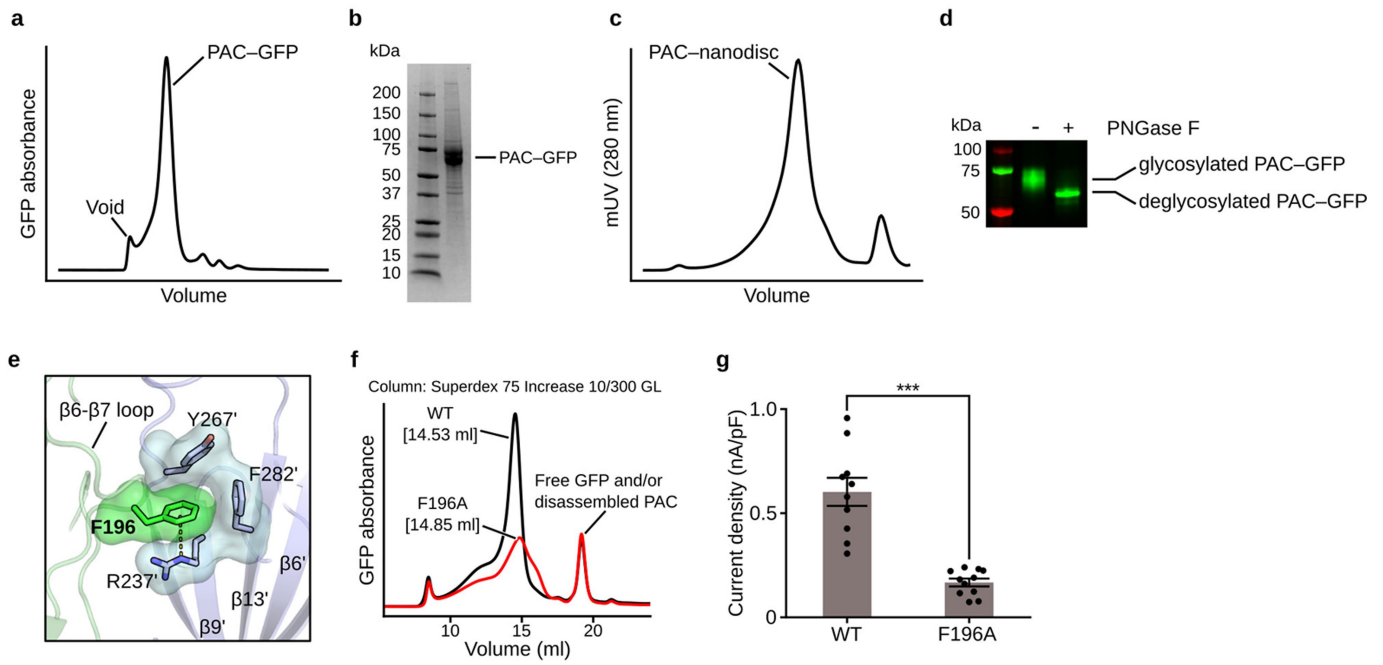
**Supplementary information** is available for this paper at <https://doi.org/10.1038/s41586-020-2875-7>.

**Correspondence and requests for materials** should be addressed to Z.Q. or W.L.

**Peer review information** *Nature* thanks Lily Jan, Stephan Kellenberger and Kenton Swartz for their contribution to the peer review of this work.

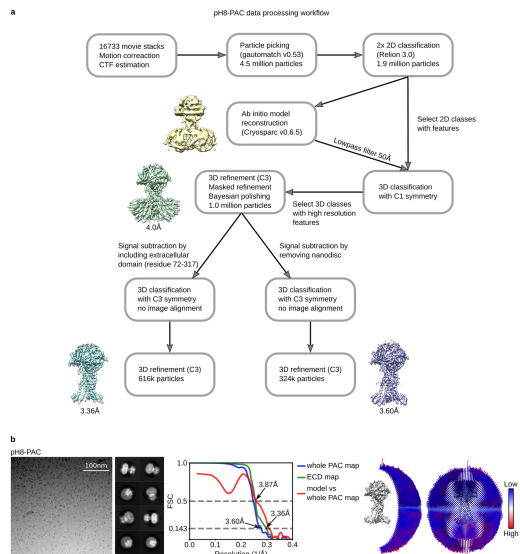
**Reprints and permissions information** is available at <http://www.nature.com/reprints>.





**Extended Data Fig. 1 | Purification of PAC and biochemical and biophysical analysis.** **a**, Fluorescence size-exclusion chromatography (FSEC) of PAC-GFP solubilized in GDN detergent. **b**, SDS-PAGE gel of purified PAC-GFP protein after metal affinity chromatography. The uncropped source gel of the image can be found in Supplementary Fig. 1a. The gel was repeated three times from different batches of purification and similar results were obtained. **c**, SEC profile of PAC in MSP3D1 nanodiscs. **d**, A deglycosylation assay of PAC-GFP with or without PNGase F treatment. The GFP and far-red signal (Alexa 488 and Alexa 680) of the gel was detected and merged using ChemiDoc imaging system (BioRad). The uncropped source gel of the image can be found in Supplementary Fig. 1b. The deglycosylation assay was repeated twice with similar results. **e**, F196 mediates intersubunit interactions by forming a

cation- $\pi$  interaction with Arg237' and hydrophobic interactions with Tyr267' and Phe282' from the adjacent subunit. The two subunits are in green and blue. **f**, FSEC traces of GFP-tagged wild-type PAC and the F196 mutant solubilized using GDN detergent. The peak position of F196A is shifted and is broader compared to the wild type, suggesting that F196A interferes with the proper assembly of PAC. **g**, The whole-cell current density of wild-type PAC and PAC(F196A) recorded at pH 4.6 with a holding potential of 100 mV. The centre error bar represents mean and s.e.m. Two-tailed unpaired *t*-test was used to determine the difference in current density between F196A and the wild type ( $P = 3.09 \times 10^{-6}$ ). D'Agostino & Pearson omnibus test was performed to check the normality of the data ( $P$  values are 0.846 and 0.349 for wild type ( $n = 10$ ) and F196A ( $n = 11$ ), respectively). \*\*\*denotes  $P < 0.001$ .

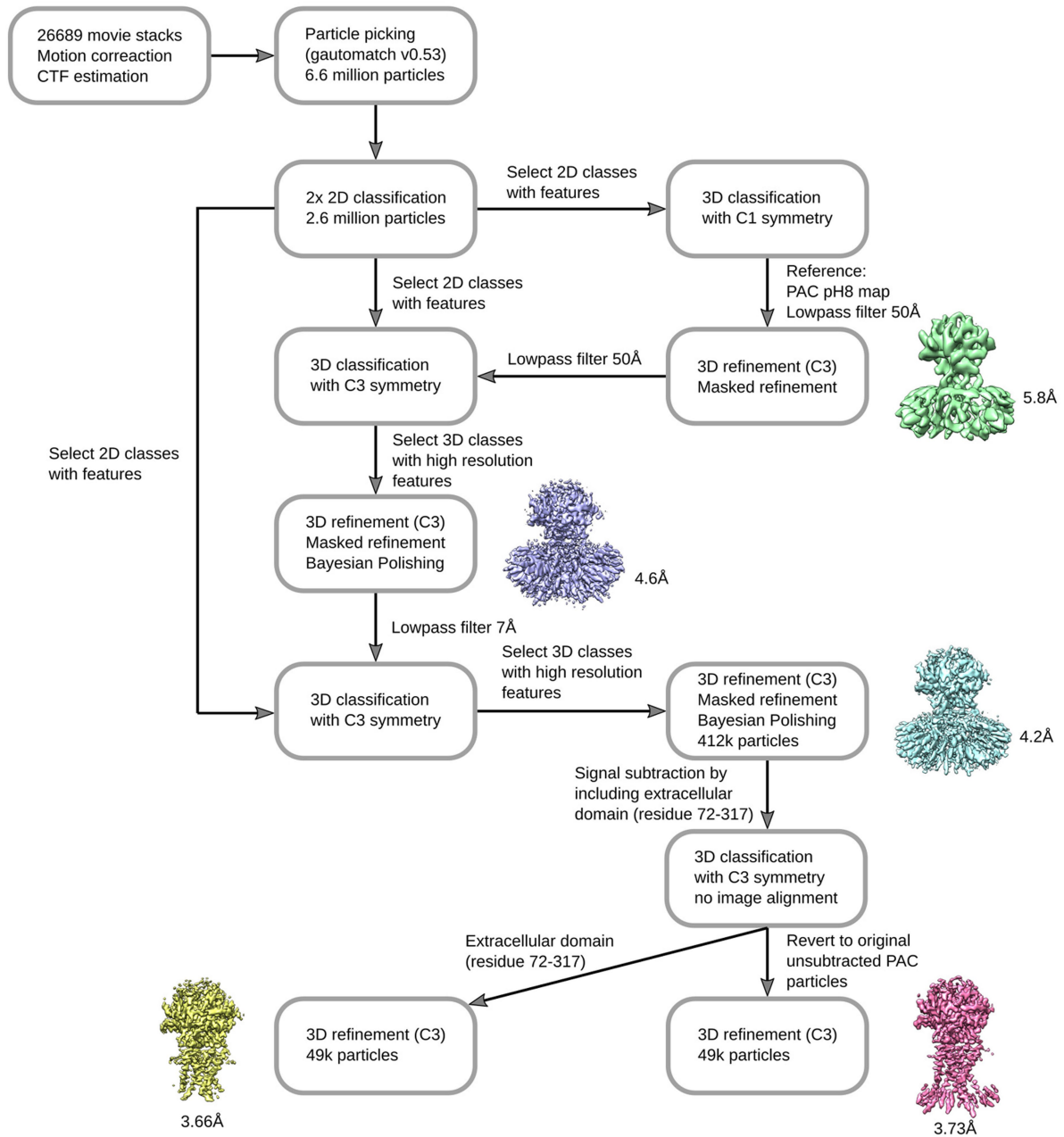


**Extended Data Fig. 2 | Workflow for cryo-EM data-processing of pH8-PAC**

**and data statistics. a,** A total of 16,733 raw movies stacks were collected and processed with motion correction, CTF estimation and particle picking. Particles were subjected to two rounds of 2D classification and a 3D classification run to obtain a homogeneous particle set. To further sort out conformational heterogeneity, we attempted to subtract and classify (1) particles without nanodiscs and (2) the ECD of PAC (residues 72–317) by using a mask. Subsequent refinement allowed us to obtain a map at 3.60-Å resolution for the entire PAC protein and 3.36-Å resolution for the ECD. **b,** Representative micrograph, 2D class averages, Fourier shell correlation (FSC) curves and angular distribution of particles used for 3D reconstruction for the pH8-PAC dataset. The gold-standard 0.143 threshold was used to determine map resolution based on the FSC curve. The threshold for model versus map correlation was 0.5 to determine the resolution.

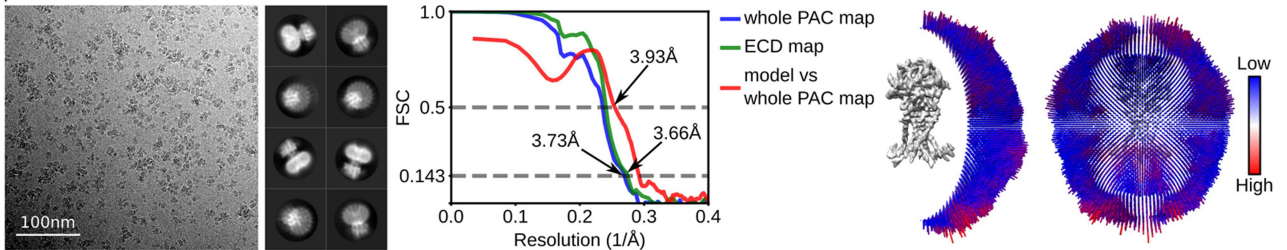
a

pH4-PAC data processing workflow



b

pH4-PAC

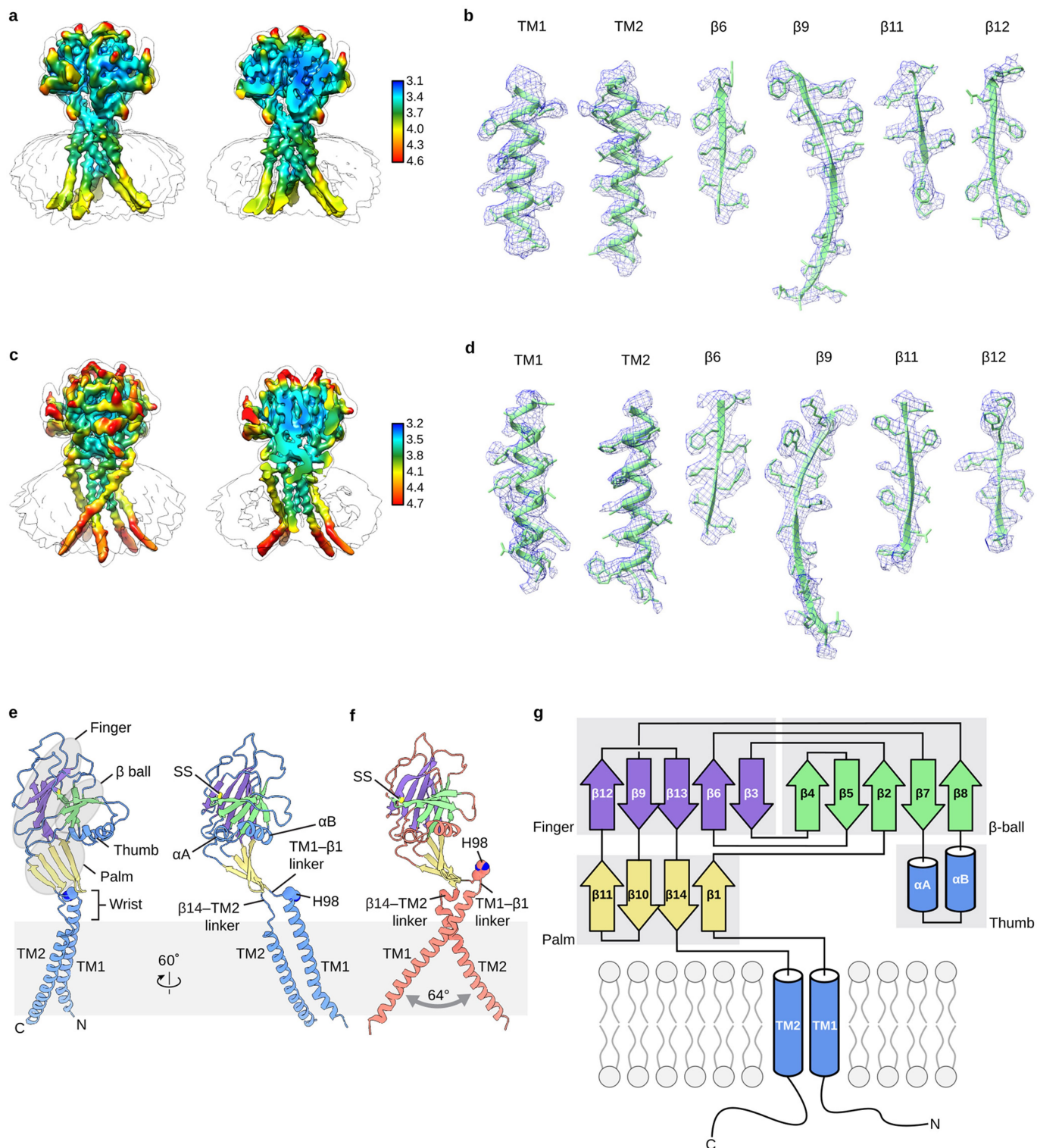


Extended Data Fig. 3 | See next page for caption.

**Extended Data Fig. 3 | Workflow for cryo-EM data-processing of pH4-PAC**

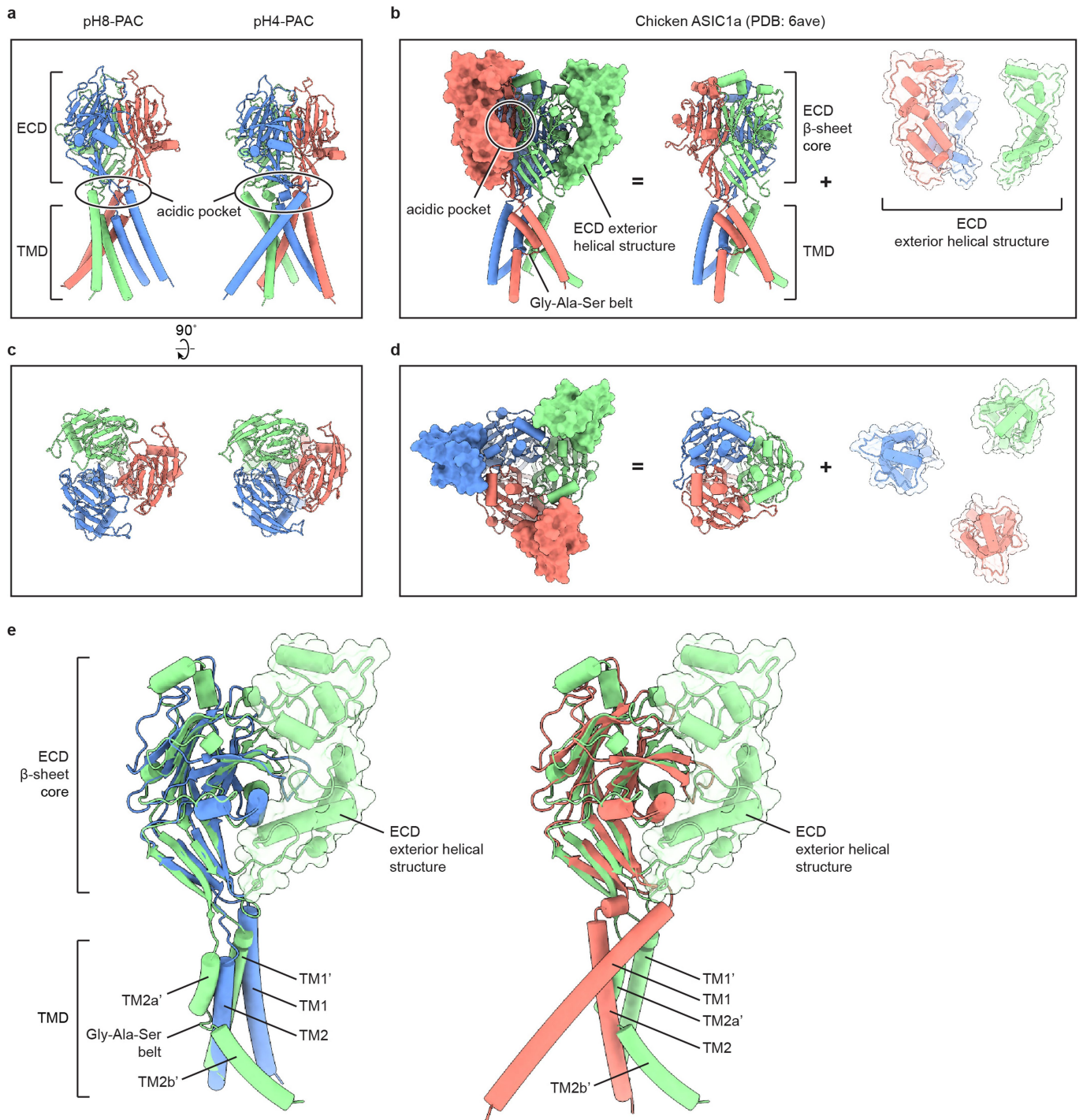
**and data statistics. a,** A total of 26,689 raw movie stacks were collected and processed with motion correction, CTF estimation and particle picking. Two rounds of 2D classification were performed to clean up junk particles. Subsequently, particles belonging to the 2D class averages with clear features were subjected to three rounds of 3D classification. The initial 3D classification was conducted by using the pH8-PAC map low-pass filter set to 50 Å as the reference. No symmetry operator was imposed in this step. After refinement with  $C_3$  symmetry, a 5.8-Å-resolution map for pH4-PAC was obtained. Subsequently, the second 3D classification job was conducted by using the 5.8-Å map as the reference and the low-pass filter set to 50 Å. We imposed  $C_3$  symmetry at this step to increase the classification efficiency. This allowed us to obtain a map at 4.6 Å after refinement. Finally, a third 3D classification job

was launched by using the 4.6-Å pH4-PAC map as the reference and the low-pass filter set to 7 Å. The  $C_3$  symmetry was also imposed. This classification pushed the resolution of the pH4-PAC map to 4.2 Å. In an effort to obtain a more homogeneous particle set, we subtracted the ECD of the pH4-PAC map (residues 72–317) and classified the refined particles without image alignment. In the end, we obtained a reconstruction of the pH4-PAC map at 3.73-Å resolution and a pH4-PAC ECD map at 3.66-Å resolution. **b,** Representative micrograph, 2D class averages, Fourier shell correlation (FSC) curves and angular distribution of particles used for 3D reconstruction for the pH4-PAC dataset. The gold-standard 0.143 threshold was used to determine map resolution based on the FSC curve. The threshold for model versus map correlation was 0.5 to determine the resolution.



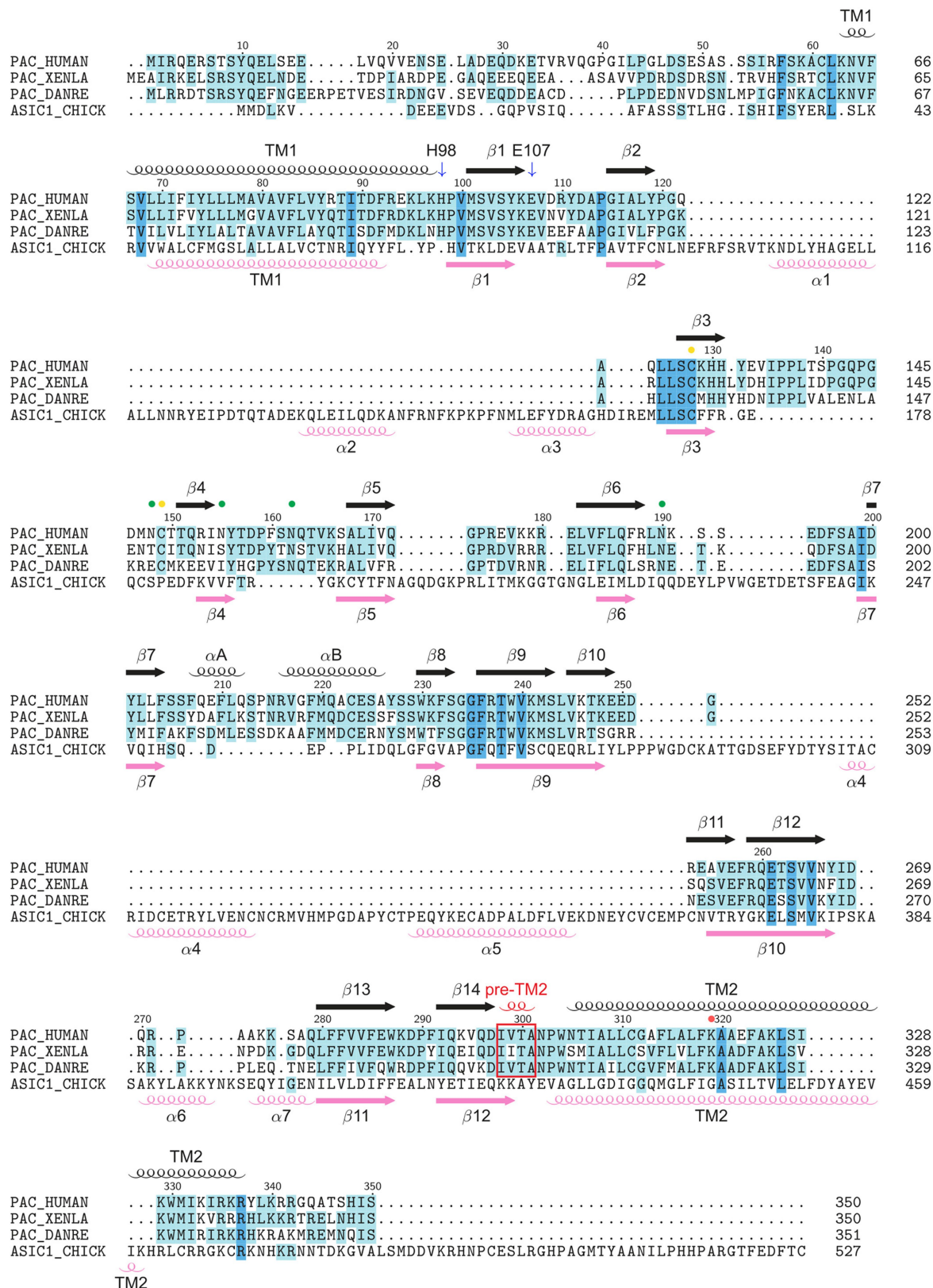
**Extended Data Fig. 4 | Local-resolution cryo-EM maps, representative densities of cryo-EM maps and domain organization of human PAC. a,** The local resolution of the pH8-PAC map. A non-sliced (left) and a sliced (right) view of the map viewed parallel to the membrane are shown. The unit for the colour key is Å. **b,** Representative densities of several secondary structural elements of pH8-PAC. The atomic model is overlaid with the density to show the side chain information. **c,** The local resolution of the pH4-PAC map. A non-sliced (left) and a sliced (right) view of the map viewed parallel to the membrane are

shown. The unit for the colour key is Å. **d,** Representative densities of several secondary structural elements of pH4-PAC. The atomic model is overlaid with the density to show the side chain information. **e,** The pH8-PAC single subunit viewed parallel to the membrane. The wrist, palm, thumb, finger and  $\beta$ -ball domains are highlighted. **f,** The pH4-PAC single subunit viewed in the same orientation as the right image of panel **e**. **g,** Domain organization of PAC. Clusters of secondary structure that form the palm, finger, thumb and  $\beta$ -ball domains are labelled.



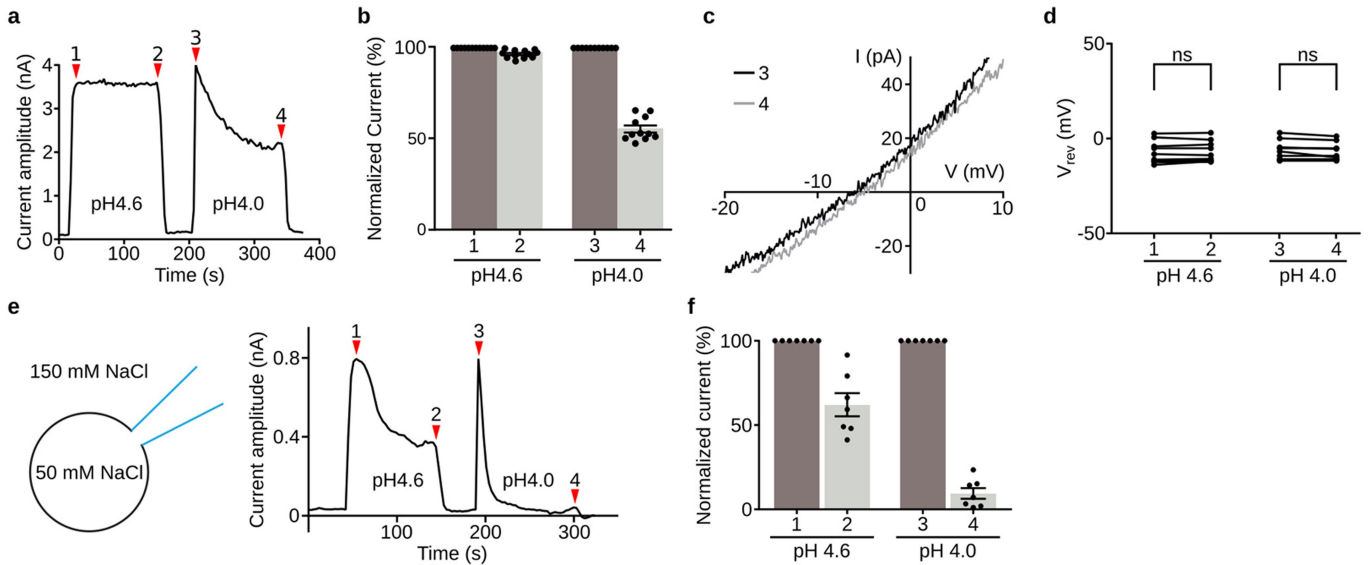
**Extended Data Fig. 5 | Comparison of the structures of PAC and ASIC.**  
**a–d**, Structural comparison of human PAC (**a**, **c**) with chicken ASIC1a (**b**, **d**) viewed parallel to the membrane (**a**, **b**) and from the extracellular side (**c**, **d**). The acidic pocket of human PAC and chicken ASIC1a are in different locations.  
**e**, Overlay of the pH8-PAC (blue) and pH4-PAC (red) single subunit with the

chicken ASIC1a (green) subunit. The ECD of ASIC1a is composed of a  $\beta$ -sheet core and the exterior helical structure. Although the  $\beta$ -sheet core shares high similarity with the human PAC structure, the chicken ASIC1a TMD is organized differently from that of the human PAC.



**Extended Data Fig. 6 | Sequence alignment of PAC homologues and ASIC.** Sequence alignment of PAC homologues (from human, frog (XENLA) and zebrafish (DANRE)) and chicken ASIC1. The ASIC1 sequence is aligned with PAC based on the structural alignment using TMalign<sup>45</sup>. Secondary structural (SS) elements of PAC are labelled at the top, whereas the SS elements of ASIC1 are indicated at the bottom. Cysteine residues mediating disulfide bonds in the

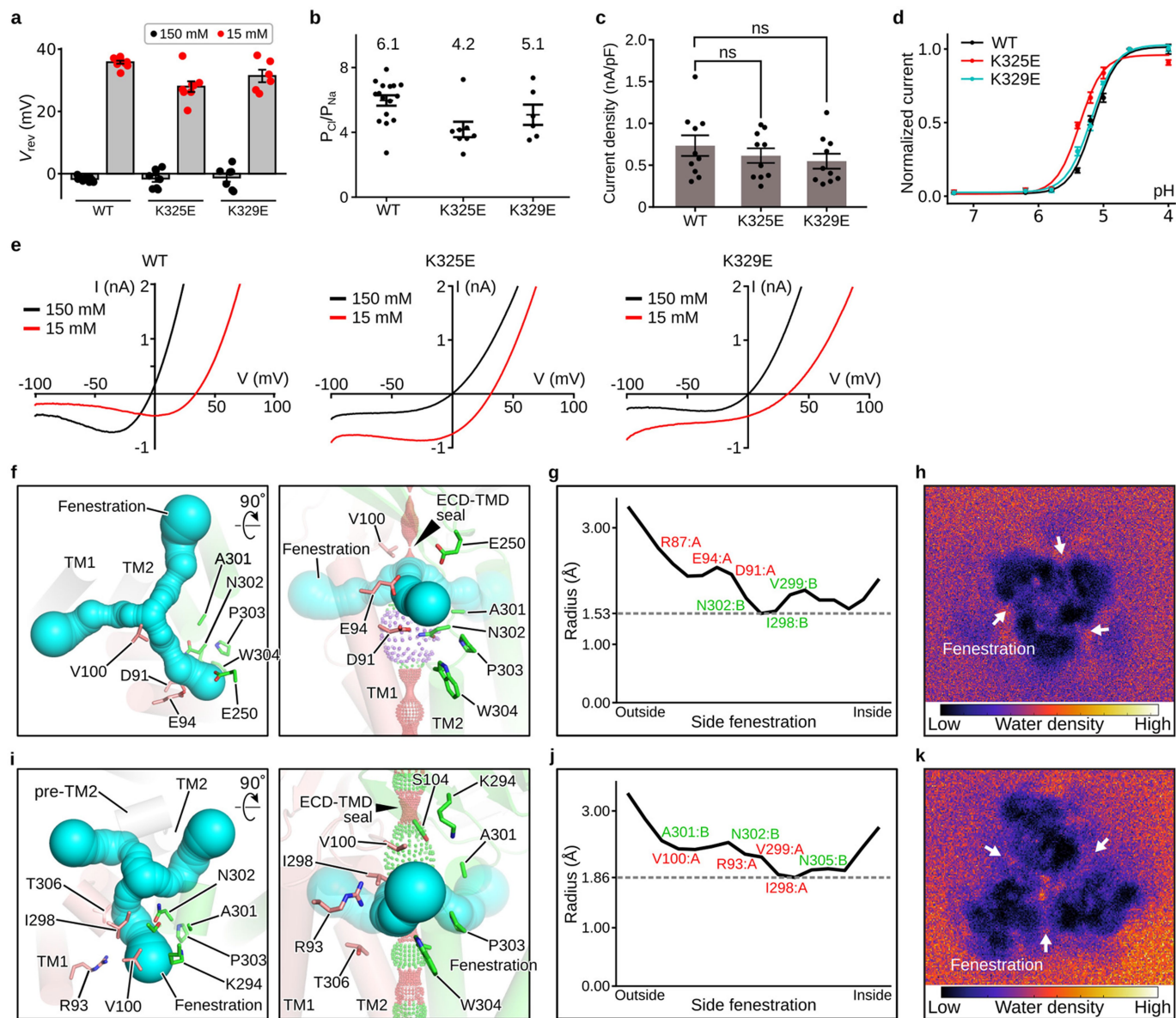
extracellular domain of PAC are marked with yellow dots. Putative N-linked glycosylation sites of PAC are highlighted with green dots. Lys319 of PAC is marked with red dots. The pre-TM2 helix observed in the pH4-PAC structure is indicated with a red frame. PAC lacks the  $\alpha 1$ ,  $\alpha 2$ ,  $\alpha 3$ ,  $\alpha 4$  and  $\alpha 5$  helices that form the ECD exterior helical structure in chicken ASIC1a, whereas the  $\alpha A$  and  $\alpha B$  helices are unique to PAC.



**Extended Data Fig. 7 | PAC channel desensitization.** **a**, A representative whole-cell current trace of PAC in wild-type HEK293 cells upon extracellular acidification at pH 4.6 and pH 4.0 with a holding potential at 100 mV. Substantial desensitization was observed during the prolonged exposure to the pH 4.0 solution (position 4 versus position 3), but not to the pH 4.6 solution (position 2 versus position 1). **b**, Quantification of PAC desensitization (pH 4.6 ( $n = 12$ ) and pH 4.0 ( $n = 11$ ) as shown in **a**. Activation and desensitization currents are normalized to the initial PAC currents. The x axis numbers correspond to the red marker location in **a**. Each data point is represented by a solid dot. The mean and s.e.m. are represented by the bar graph. **c**, Representative whole-cell current-voltage traces of PAC at the beginning (position 3 in **a**) and the end (position 4 in **a**) of pH 4.0 treatment. **d**, Reversal potential of PAC at the beginning and the end of pH 4.6 and pH 4.0 treatment, respectively ( $n = 9$ ). Two-tailed paired  $t$ -test was used to determine significance ( $P$  values are 0.361

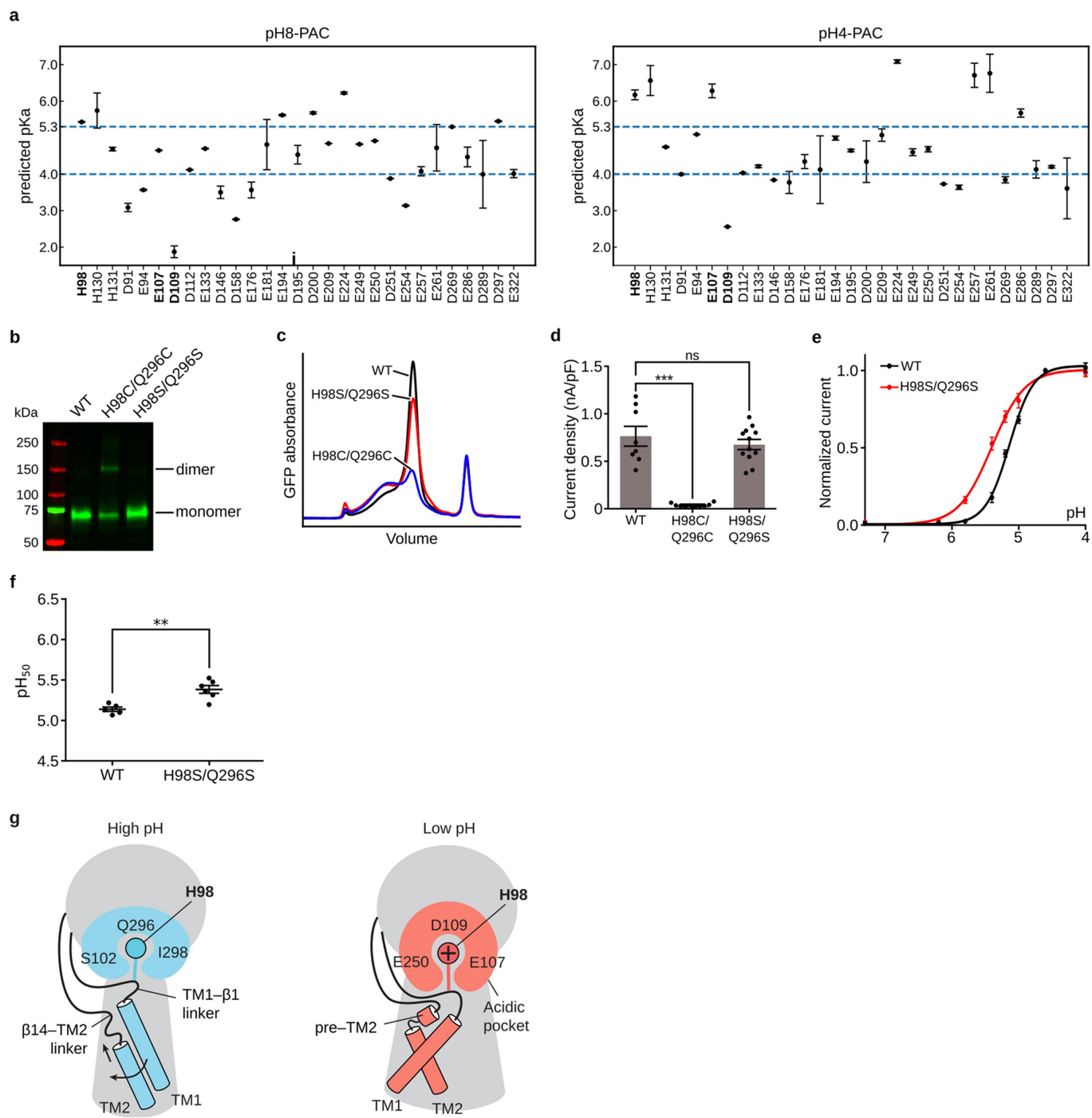
and 0.077 for pH 4.6 and pH 4.0, respectively). D'Agostino & Pearson omnibus test was performed to check the normality of the data ( $P$  values are 0.673 and 0.335 for pH 4.6 and pH 4.0 conditions, respectively). NS indicates  $P > 0.05$ . **e**, Whole-cell patch-clamp recording configuration with 50 mM NaCl pipette solution and 150 mM bath solutions (scheme depicted on the left). This creates the concentration gradient necessary to observe any potential PAC current at 0 mV. Owing to the small amplitude of endogenous PAC current at 0 mV, we transfected PAC cDNA in PAC knockout HEK293 cells. The representative whole-cell current trace of PAC upon acidification at 0 mV is shown on the right. Location 1 and 3 represent initial activation of PAC immediately after acidic buffer treatment. Location 2 and 4 represent desensitized PAC after prolonged acidic buffer treatment. **f**, The desensitized currents (position 2 and 4 in **e**) are normalized to the initial PAC currents (position 1 and 3 in **e**). The desensitized data currents are represented by the normalized average  $\pm$  s.e.m.





**Extended Data Fig. 8 | Lateral fenestration and ion selectivity of PAC.** **a**, The reversal potential ( $V_{rev}$ ) of wild-type PAC, PAC(K325E) and PAC(K329E) at 150 mM NaCl (black) or 15 mM NaCl (red) in the bath solution (internal solution contains 150 mM NaCl). The bar graph represents the mean and s.e.m. ( $n = 16$  (wild type),  $n = 8$  (K325E) and  $n = 6$  (K329E)). Individual data points are shown as dots. The same data points for the wild type were also used in Fig. 3i for comparison with K319E. **b**, The relative  $Cl^-/Na^+$  permeability for wild-type PAC ( $n = 16$ ), and K325E ( $n = 8$ ) and K329E ( $n = 6$ ) mutants calculated from the pH-5-induced current at 100 mV. The centre and error bar represent the mean and s.e.m. of the permeability ratio. Individual data points are shown as solid dots. The same data points for the wild type were also used in Fig. 3j for comparison with K319E. The average  $P_{Cl^-}/P_{Na^+}$  permeability values are indicated for each construct. **c**, The current density of wild-type PAC ( $n = 10$ ), and K325E ( $n = 10$ ) and K329E mutants ( $n = 10$ ) at pH 4.6 with a holding potential of 100 mV. The bar graph shows the average normalized current density  $\pm$  s.e.m. One-way ANOVA with Bonferroni post-hoc test was used to determine the significance ( $P$  values are 0.832 and 0.416 for K325E and K329E, respectively). D'Agostino & Pearson omnibus test was performed to check the normality of the data ( $P$  values are 0.255, 0.153 and 0.293 for the wild type and K325E and K329E mutants, respectively). NS indicates  $P > 0.05$ . **d**, The pH dose-response curve of

wild-type PAC, PAC(K325E) and PAC(K329E). The currents are normalized to those at pH 4.6 ( $n = 8$  (wild-type PAC),  $n = 6$  PAC(K325E) and  $n = 7$  (PAC(K329E))). The currents at different pH are represented by the average normalized currents  $\pm$  s.e.m. A nonlinear fitting to a sigmoidal dose-response curve is generated for each construct. **e**, Representative whole-cell patch-clamp recording at pH 5.0 with 150 mM NaCl pipette solution and 150 mM (black) or 15 mM NaCl (red) bath solutions. The current-voltage relationship of wild-type (left), K325E (middle) and K329E (right) PAC in two different bath solutions are plotted. The same wild-type traces were also shown in Fig. 3j (left) for comparison with K319E. **f, i**, The pH8-PAC and pH4-PAC extracellular fenestration viewed from the extracellular side (left) and parallel to the membrane (right), respectively. Residues forming the fenestration are shown in sticks, including three negatively charged residues (Asp91, Glu94 and Glu250) for pH8-PAC and two positively charged residues (Arg93 and Lys294) for pH4-PAC. **g, j**, Radius of the fenestration tunnel, estimated by CAVER v.3.0, for pH8-PAC (**g**) and pH4-PAC (**j**). The horizontal line marks the smallest radius along the tunnel. The residues lining the fenestration tunnel are marked. **h, k**, Fenestration water-density plot for pH8-PAC (**h**) and pH4-PAC (**k**) from a 100-ns MD simulation. Water molecules in the Z range of the side fenestration site are projected to the X/Y plane and are shown as a 2D histogram.



**Extended Data Fig. 9** | See next page for caption.

# Article

**Extended Data Fig. 9 | His98 is involved in PAC pH sensing.** **a**,  $pK_a$  prediction of titratable residues for the pH8 and pH4 structures of human PAC. The mean and error bar (standard deviation) are calculated based on 1,000 fixed-backbone rotamer ensembles generated from each structure (see Methods). **b**, SDS gel of GFP-tagged wild-type PAC, PAC(H98C/Q296C) and PAC(H98S/Q296S). A dimeric band is observed for the H98C/Q296C mutant, but not for the wild type and the H98S/Q296S mutant. The unedited source gel of the image can be found in Supplementary Fig. 1c. The gel was independently repeated twice with similar results. **c**, The FSEC profile of GFP-tagged wild-type PAC, PAC(H98C/Q296C) and PAC(H98S/Q296S) solubilized using GDN detergent. **d**, The whole-cell current density of wild-type PAC, PAC(H98C/Q296C) and PAC(H98S/Q296S) recorded at pH 5.0 at 100 mV. The bar graph shows the average current density (nA/pF)  $\pm$  s.e.m. Each individual data point represents a cell ( $n = 8$  (wild type),  $n = 10$  (H98C/Q296C) and  $n = 12$  (H98S/Q296S)). Two-tailed unpaired  $t$ -test was used to determine the difference in current density compared to the wild type ( $P$  values are  $1.08 \times 10^{-6}$  for H98C/Q296C and 0.321 for H98S/Q296S). D'Agostino & Pearson omnibus test was performed to check the normality of the data ( $P$  values are 0.328, 0.154 and

0.727 for the wild type and the H98C/Q296C and H98S/Q296S mutants, respectively). **e**, The pH dose-response curve of wild-type PAC and PAC(H98S/Q296S). The currents are normalized to those at pH 4.6 ( $n = 5$  (wild-type PAC);  $n = 6$  (PAC(H98S/Q296S))). A nonlinear fitting to a sigmoidal dose-response curve is generated for each construct. Bar plot shows the mean  $\pm$  s.e.m. **f**, The  $pH_{50}$  of wild-type PAC and PAC(H98S/Q296S) estimated from the pH dose-response curve. The centre and bar represent the estimated  $pH_{50}$  and s.e.m. from the nonlinear fitting in **e**. Two-tailed Mann-Whitney test was used to determine the significance ( $P = 0.0087$ ). **g**, The proposed pH-sensing mechanism for PAC. At high pH, the deprotonated His98 residue is surrounded by Gln296, Ser102 and Iso298, and TM1 pairs with TM2 from the same subunit. At low pH, the protonated His98 residue undergoes a conformational change and moves into an acidic pocket. As a result, TM1 dissociates from the resting interface and rotates to interact with TM2 of the adjacent subunit. For all panels, NS indicates  $P > 0.05$ , \*\* denotes a  $P$  value between 0.01 and 0.001 and \*\*\* denotes  $P < 0.001$ ;  $n$  represents measurements from biologically independent cells.

Extended Data Table 1 | Cryo-EM data collection, refinement and validation statistics

	pH8-PAC	pH4-PAC
<b>Data collection and processing</b>		
Magnification	130,000	130,000
Voltage (kV)	300	300
Electron exposure ( $e^-/\text{\AA}^2$ )	49.6	49.6
Defocus range ( $\mu\text{m}$ )	-1.2 to -1.9	-1.2 to -1.9
Pixel size ( $\text{\AA}$ )	1.026	1.026
Symmetry imposed	C3	C3
Initial particle images (no.)	4,515,826	6,647,983
Final particle images (no.)	323,766	48,551
Map resolution ( $\text{\AA}$ )	3.60	3.73
FSC threshold	0.143	0.143
Map resolution range ( $\text{\AA}$ )	3.60 – 246.2	3.73 – 246.2
<b>Refinement</b>		
Initial model used (PDB code)	<i>De novo</i>	<i>De novo</i>
Model resolution ( $\text{\AA}$ )		
FSC threshold	3.87	3.93
Map sharpening <i>B</i> factor ( $\text{\AA}^2$ )	-180.05	-148.66
Model composition		
Non-hydrogen atoms	6432	6573
Protein residues	834	861
Ligands	0	0
R.m.s. deviations		
Bond lengths ( $\text{\AA}$ )	0.004	0.004
Bond angles ( $^\circ$ )	0.627	0.617
Validation		
MolProbity score	1.87	2.07
Clashscore	11.12	16.75
Poor rotamers (%)	0.00	0.00
Ramachandran plot		
Favored (%)	95.65	95.09
Allowed (%)	4.35	4.91
Disallowed (%)	0.00	0.00

## Reporting Summary

Nature Research wishes to improve the reproducibility of the work that we publish. This form provides structure for consistency and transparency in reporting. For further information on Nature Research policies, see [Authors & Referees](#) and the [Editorial Policy Checklist](#).

### Statistics

For all statistical analyses, confirm that the following items are present in the figure legend, table legend, main text, or Methods section.

n/a Confirmed

- The exact sample size ( $n$ ) for each experimental group/condition, given as a discrete number and unit of measurement
- A statement on whether measurements were taken from distinct samples or whether the same sample was measured repeatedly
- The statistical test(s) used AND whether they are one- or two-sided  
*Only common tests should be described solely by name; describe more complex techniques in the Methods section.*
- A description of all covariates tested
- A description of any assumptions or corrections, such as tests of normality and adjustment for multiple comparisons
- A full description of the statistical parameters including central tendency (e.g. means) or other basic estimates (e.g. regression coefficient) AND variation (e.g. standard deviation) or associated estimates of uncertainty (e.g. confidence intervals)
- For null hypothesis testing, the test statistic (e.g.  $F$ ,  $t$ ,  $r$ ) with confidence intervals, effect sizes, degrees of freedom and  $P$  value noted  
*Give  $P$  values as exact values whenever suitable.*
- For Bayesian analysis, information on the choice of priors and Markov chain Monte Carlo settings
- For hierarchical and complex designs, identification of the appropriate level for tests and full reporting of outcomes
- Estimates of effect sizes (e.g. Cohen's  $d$ , Pearson's  $r$ ), indicating how they were calculated

*Our web collection on [statistics for biologists](#) contains articles on many of the points above.*

### Software and code

Policy information about [availability of computer code](#)

Data collection

SerialEM 3.7, ClampFit 10.6

Data analysis

Gctf-1.06, ctffind-4.1.10, Gautomatch-0.56, Relion-3.0, CryoSparc-v0.6.5, coot-0.8.9.2, pymol-2.3.2, Motioncor2-1.2.1, phenix.real\_space\_refine\_dev\_3500, phenix.molprobrity\_dev\_3500, UCSF chimera\_1.13.1, UCSF chimeraX\_0.91, GraphPad Prism 6 and 7, ClampFit\_10.6, GROMACS version 2019.2, OPM server ([https://opm.phar.umich.edu/ppm\\_server](https://opm.phar.umich.edu/ppm_server)), CHARMM-GUI (<http://www.charmm-gui.org/>), Rosetta 2020.08.61146, propka3.1, TMalign v20190822

For manuscripts utilizing custom algorithms or software that are central to the research but not yet described in published literature, software must be made available to editors/reviewers. We strongly encourage code deposition in a community repository (e.g. GitHub). See the Nature Research [guidelines for submitting code & software](#) for further information.

### Data

Policy information about [availability of data](#)

All manuscripts must include a [data availability statement](#). This statement should provide the following information, where applicable:

- Accession codes, unique identifiers, or web links for publicly available datasets
- A list of figures that have associated raw data
- A description of any restrictions on data availability

The cryo-EM density map and coordinates of pH8-hsPAC and pH4-hsPAC have been deposited in the Electron Microscopy Data Bank (EMDB) under accession numbers EMD-22403 and EMD-22404 and in the Research Collaboratory for Structural Bioinformatics Protein Data Bank under accession codes 7JNA and 7JNC.

## Field-specific reporting

Please select the one below that is the best fit for your research. If you are not sure, read the appropriate sections before making your selection.

Life sciences       Behavioural & social sciences       Ecological, evolutionary & environmental sciences

For a reference copy of the document with all sections, see [nature.com/documents/nr-reporting-summary-flat.pdf](https://www.nature.com/documents/nr-reporting-summary-flat.pdf)

## Life sciences study design

All studies must disclose on these points even when the disclosure is negative.

Sample size	Sample size was not pre-determined for the study. All the electrophysiology experiments were repeated at least five times using different cells. The sample size was determined based on the consistence/variability of the recordings. Overall, the samples sizes were deemed sufficient based on the clearly visible effects of the mutations on the overall distribution of data points within and between each group (The sample standard deviation is usually much smaller than the effect we are aiming to test). However, we acknowledge that our current sample size may not be sufficient to detect small effect that may be present in some of the comparisons, leading us to accept the null hypothesis.
Data exclusions	No data was excluded from the analysis.
Replication	We have done each group of experiment with several batches of cells and different transfection, to ensure reproducibility within the lab. The number biologically independent experimental replications is indicated in the figure legend. For electrophysiology recordings, the number is at least 5. For SDS PAGE gel experiments, they were repeated at least twice.
Randomization	Our experiment is not randomized. For electrophysiology experiments, cells with GFP fluorescence (proteins were GFP-tagged) were randomly selected. Other experiments including protein expression, solubilization test, protein purification, deglycosylation assay, and cryo-EM grids preparation and data collection were repeated multiple time; each time, proteins from different random batches were used.
Blinding	The investigators were not blinded; it was not technically or practically feasible to do so for cryo-EM or patch-clamp studies.

## Reporting for specific materials, systems and methods

We require information from authors about some types of materials, experimental systems and methods used in many studies. Here, indicate whether each material, system or method listed is relevant to your study. If you are not sure if a list item applies to your research, read the appropriate section before selecting a response.

### Materials & experimental systems

### Methods

n/a	Involved in the study	n/a	Involved in the study
<input checked="" type="checkbox"/>	<input type="checkbox"/> Antibodies	<input checked="" type="checkbox"/>	<input type="checkbox"/> ChIP-seq
<input type="checkbox"/>	<input checked="" type="checkbox"/> Eukaryotic cell lines	<input checked="" type="checkbox"/>	<input type="checkbox"/> Flow cytometry
<input checked="" type="checkbox"/>	<input type="checkbox"/> Palaeontology	<input checked="" type="checkbox"/>	<input type="checkbox"/> MRI-based neuroimaging
<input checked="" type="checkbox"/>	<input type="checkbox"/> Animals and other organisms		
<input checked="" type="checkbox"/>	<input type="checkbox"/> Human research participants		
<input checked="" type="checkbox"/>	<input type="checkbox"/> Clinical data		

## Eukaryotic cell lines

Policy information about [cell lines](#)

Cell line source(s)	Sf9 cells, tsA201 cells and HEK293 cells were purchased from ATCC
Authentication	The cells were purchased and routinely maintained in our lab. They were not authenticated experimentally for these studies.
Mycoplasma contamination	Sf9 cells, tsA201 cells and HEK293 cells were tested negative form Mycoplasma contamination
Commonly misidentified lines (See <a href="#">ICLAC</a> register)	No commonly misidentified lines were used